CHAPTER 2

LITERATURE REVIEW

2.1 Introduction

A large number of topics on the vapor explosion have been studied for more than four decades. In fact the vapor explosion can occur naturally between hot magma and ground water [6], which resulted in a great damage done to the earth. The vapor explosion was first noted as the industrial hazards in the aluminum industry [7], the pulp and paper industry, and the transportation of the liquefied natural gas. In the nuclear industry, the core meltdown accident was postulated to cause the vapor explosion [8].

The vapor explosion involves the rapid conversion of energy from one form to another. Before the explosion is initiated, the energy must be stored in a form that exists for some time without significant energy dissipation. This is called metastable stage [1] as shown in Fig. 2.1.

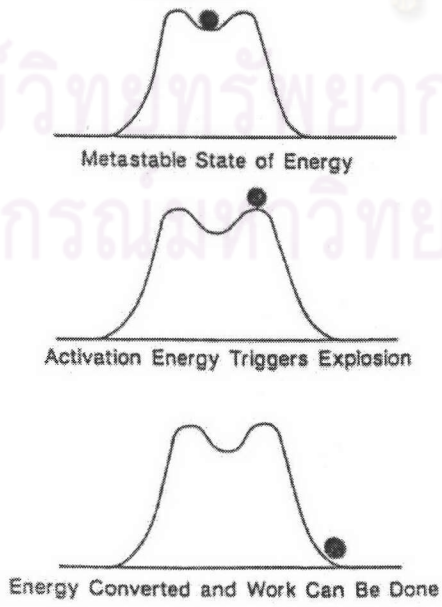

Fig. 2.1 Conceptual phases of an explosion [1]

The explosion may then be triggered by some relatively small amount of activation energy and initiates the rapid conversion of the system energy into some form that can do work on the surroundings, such as the kinetic energy. Generally, the process of the explosion has been conceptually subdivided into four phases of (1) mixing, (2) triggering and local fuel fragmentation, (3) explosion propagation and (4) expansion and work done.

A thermodynamic interpretation [9] after the triggering in the conceptual phases is shown in Fig. 2.2. In PV diagram the cold liquid (C) starts from point 0. The pressure increases to an intermediate state 1 due to rapid heat transfer from the hot liquid (H) at an almost constant volume. Then the liquid C expands against the atmospheric pressure or a closed chamber P_a and continues to state 2. The work is done during the expansion. If the heat transfers slowly from the hot liquid to the cold liquid, the produced pressure will increase slowly and cause the pressure different, P_c-P_a, so small. Hence, the small work occurs in a longer period of time.

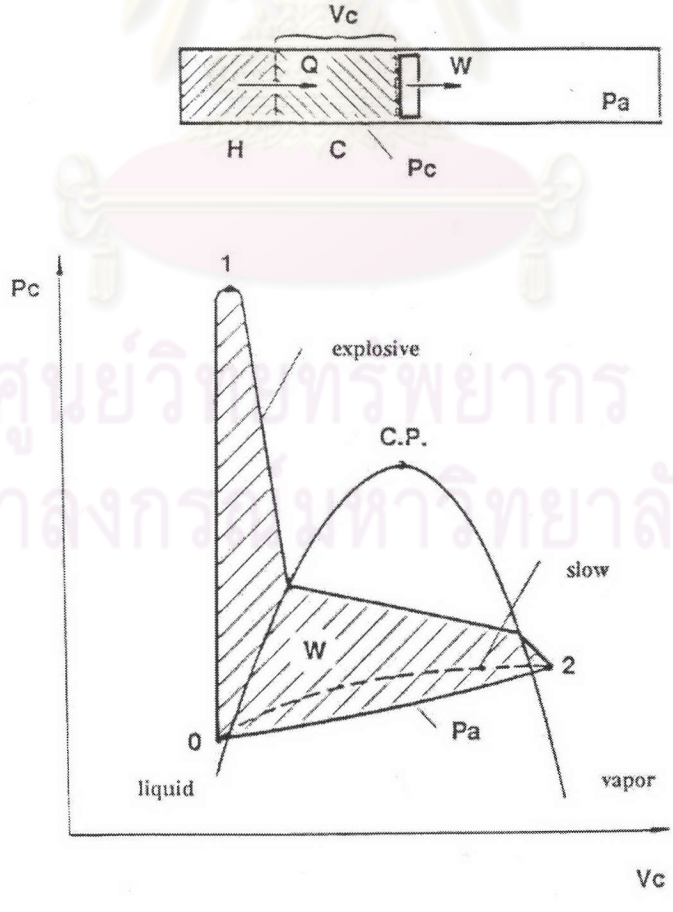

Fig. 2.2 Process of a vapor explosion in a pressure-volume diagram [9]

Many researches on the vapor explosion have many different objectives. These objectives are tested either by the experiment or by the theoretical modeling or both. The briefed review of the experiment and modeling will be described in this chapter.

2.2 Experimental work

The experimental works can be divided into two groups in terms of the scale of the experiments, the large-scale experiments and the small scale experiments. The scale may be referred by the initial mass of both liquids used in the experiments. Sometimes, it is referred to the spatial propagation when compared with the dimension of the local interaction. In any case, it is the objectives of the study that define the scale of the experiments.

Many research groups in the large-scale experiments attempt (1) to proof the possibility of the explosion under the given initial conditions and geometry for the industrial facility, (2) to investigate the spatial propagation of explosion in the large system, (3) to estimate the energy conversion from thermal energy to mechanical energy, and (4) to determine the scale effects in regard to the real system. On the other hand, the other groups in the small- scale experiments try to explain the possible fast and sometimes invisible mechanism that causes the explosion.

2.3 Large Scale Experiments

As stated in Chapter 1, many large-scale test facilities have been constructed during the past decades. Two notable facilities are the FARO facility in Italy (it is now subsumed as part of EU program and is being operated by CEA, France) and the ALPHA facility in Japan. Many different materials (fuel and coolant) and conditions used in many large-scale experiments have been tested. The materials and conditions selected may depend on the criteria of the study, the industrial application, or the simulating material in order to avoid the use of the radioactive molten nuclear fuel. Some experiments used a number of hot metal spheres dropping into the water pool instead of the hot liquid [10]. These experiments are supposed to characterize the real nuclear severe accident.

Magallon et al. [11] performed two experiments by pouring 100-kg-scale molten UO2 into the liquid sodium in the test section TERMOS of the FARO facility. Its arrangement is shown in Fig. 2.3 and the test instrument is shown in Fig. 2.4.

The first test (T1) used the release channel diameter of 50 mm, molten UO2 mass of 110 kg, Weber number of order 10,000, initial sodium temperature of 400°C, initial sodium height of 2.5 meters, and UO2 temperature just before contacting ~3000°C. The other test T2 used the larger release channel with diameter of 80 mm, molten UO2 mass of 140 kg.

In their experiments, the pressure transducer installed in the cover gas measured the pressure profile as shown in Fig. 2.5. Four pressure transducers measured the pressure in liquid sodium and these pressure profiles occurred in the liquid sodium are shown in Fig. 2.6 (a) and (b). The peak pressure in cover gas is 0.47 MPa. The peak duration is 1.2 seconds. The major peak pressure in cover gas from T1 and T2 exhibits almost exactly the same shape and duration. They suggested that the melt mass involved in the event is nearly equal.

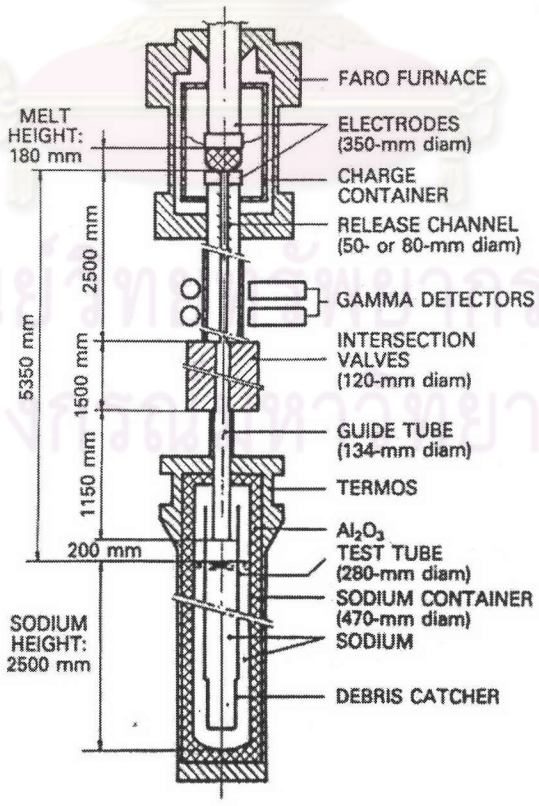

Fig. 2.3 KROTOS experimental arrangement [11]

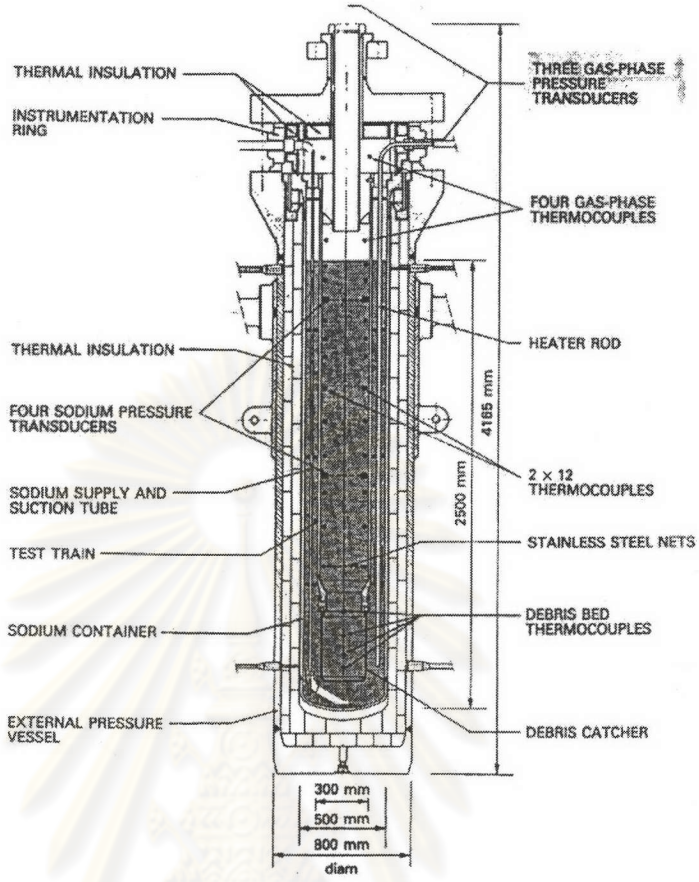

Fig. 2.4 Test instrument [11]

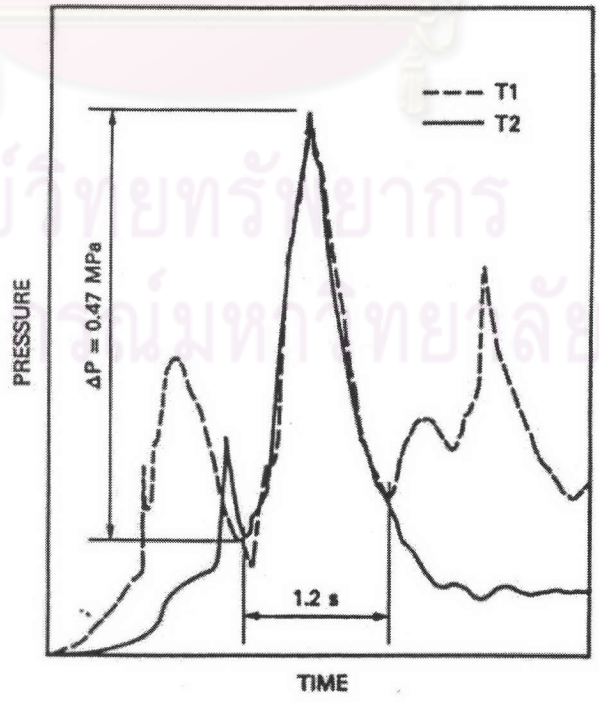

Fig. 2.5 Pressure peak in cover gas from two tests, T1 and T2 [11]

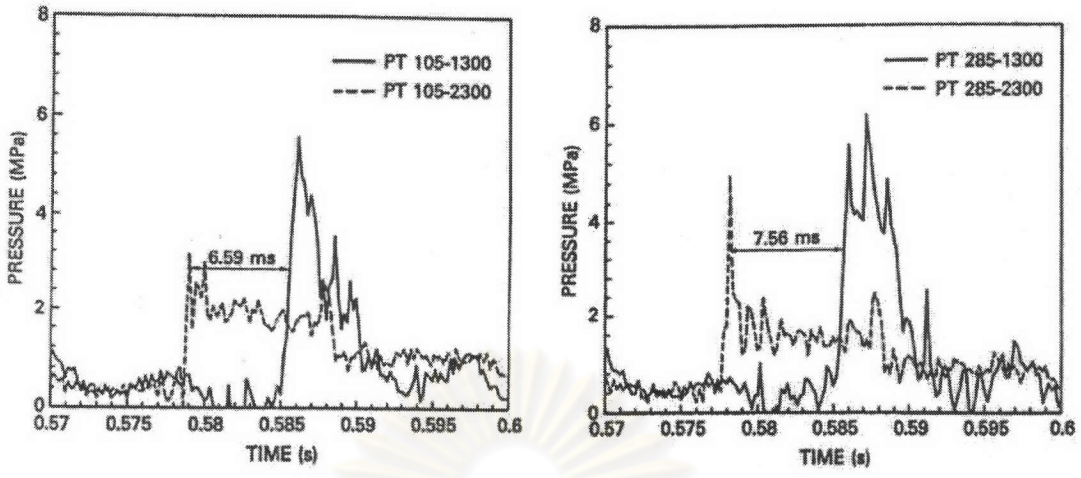

(a) (b)

Fig. 2.6 First T2 sodium pressure peak at an angular of
(a) 105 deg and (b) 285 deg [11]

2.3.1 Spatial Propagation

The pressure peaks detected at the different levels in the liquid sodium show the short rise time (<1ms) and very large amplitude (6 MPa). The peaks have a delay time of ~7 ms. Assuming that these signals refer to the same event originating near the 2300-mm level and propagating downward, this gives a propagation velocity equal to 143 m/s. The researchers suggested that the shocks occurred and associated with the vapor explosion.

2.3.2 Debris and conversion ratio

After the experiment, the debris structure in the debris catcher as shown in Fig. 2.7 was observed and was separated into two main zones for T1. The first zone went from the bottom to about two-thirds of the debris height (~35 kg of debris upon a mean height of 160 mm). It presented an increasing number of voids from the bottom to the top. The second zone was above the first zone (~25 kg of debris upon a mean height of 80 mm) and it looked more dense. The rest of the melt (~40 kg) was found deposited all over the inner surface at the top of the test vessel. It was evidence that a significant part of this UO2 was still molten when it "splashed." For T2, the debris structure was very similar. A total of 45 kg of debris was collected in the

catcher, ~15 kg was found splashed in a way similar to that T1, and ~80 kg was stuck in the intersection valve. The researchers suggested that the first ~35 kg in T1 resulted in the first pressure peak in cover gas. As seen in Fig 2.5, the T2 major peak exhibits exactly the same shape and duration as the corresponding one in T1, indicating that the same melt quantity was probably involved in the event. Then the second pressure peak in T2 should have been involved with ~10 kg and so was the second peak in T1. They also assumed that the initial cover gas volume was compressed isentropically by the expanding vapor from the pressure just before the FCI pressure rose to the maximum FCI pressure. The total mechanical energy results were 75 and 40 kJ for T1 and T2, respectively. Taking the energy of the UO2 melt as 1.55 MJ/kg, the conversion ratios were 0.08% for T1 and 0.06% for T2. And the conversion ratio was 0.16% for the second peak of both tests.

Fig. 2.7 Axial cut of the T1 debris bed [11]

The results from the experiment mentioned above are typical results but more informative than many other large-scale tests. The peak pressure detected in the cover gas is much less than the peak pressure appeared in the liquid. Two peak pressures in the liquid rise with a delay time due to propagation, assuming that the peaks occur from the same event. In addition, these two peak pressures show the progressive magnitude after a propagating distance. The debris also provides the information on the interaction mass. The isentropic compression of the initial cover gas volume inside the closed vessel is an assumption to find out the mechanical energy yield. With the energy of the interaction mass, the conversion ratio can be estimated.

Bang [9] performed a study of the stratified vapor explosions. In his work, the water is the molten fuel while the liquid nitrogen or freon-12 is the coolant. The experiment of the water and the liquid nitrogen interaction will be described here. The layout of the experimental apparatus is shown in Fig. 2.8.

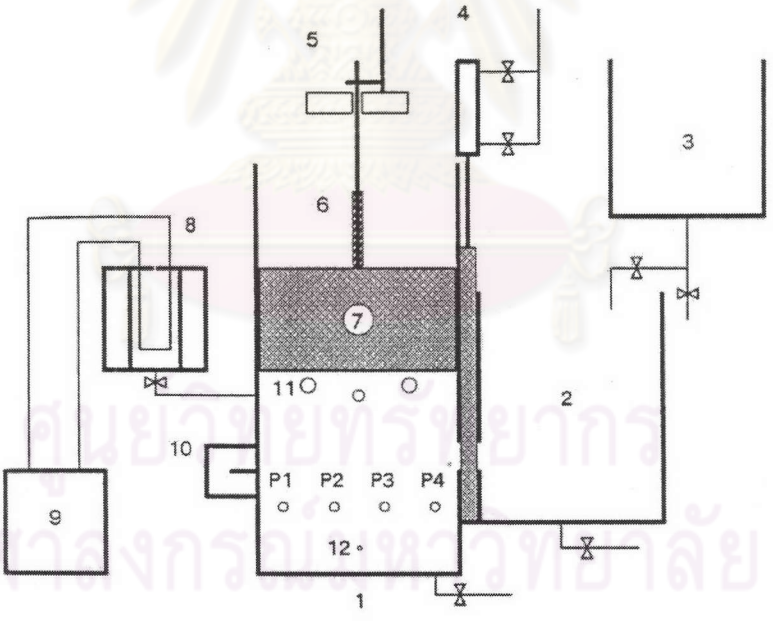

1. Interaction vessel 2. Second liquid reservoir 3. Dewer
4. Pneumatic cylinder 5. Slug displacement recorder 6. Spring
7. Slug 8. Water heater 9. Constant temperature bath
10. Electromagnet 11. Vapor vent holes 12. Thermocouple
P1–P4. Pressure transducers

Fig. 2.8 Schematic of experimental apparatus in water/LN2 experiments [9]

The interaction is designed to occur in an open-topped, narrow vessel. The inner diameter is 20 cm long and 2.5 cm wide. The height of the vessel is initially 65 cm. This height was designed to measure the explosion work by allowing a slug to move vertically inside the vessel during the expansion phase of the explosion. The front of the vessel is covered by a transparent plate (Plexiglas, Lexan) to allow for the visual observation using a high-speed camera. The vessel is designed such that 10 cm of the bottom is filled with the heavier liquid (water) and the lighter liquid (nitrogen) is introduced from its reservoir into the vessel at the level of the top surface of the heavier liquid. The reservoir is attached at one side of the interaction vessel and the liquid nitrogen flows pass the slide gate opened by a fast acting pneumatic cylinder. The cylinder is designed to close the gate just before the triggering. The reservoir is designed so that it allows the liquid nitrogen to flood on the water in the vessel by the hydrostatic pressure with up to 15 cm high. The external trigger provides a pressure shock to the vapor film interface. The trigger is located opposite to the gate. It is designed to collapse the film locally and trigger the interaction. The film collapsing process will move from the triggering point to the opposite side of the vessel and is supposed to be observed. Four pressure transducers are installed under the water surface to measure the interaction pressure. The trigger pressure is shown in Fig. 2.9 and its pressures recorded by the four transducers are shown in Fig. 2.10

When LN2 floods on the water, both liquids come into contact and cause a vapor film boiling. The film is stable along the interface. This process takes about 4~5 seconds before the triggering is initiated. After the triggering, the film collapses and the explosion occurs. The movie taken with the high-speed camera shows this as the blurred image behind the shock front. The depth of intermixing is not big enough to be identified clearly in the movie shown in Fig. 2.11. The pressure records in Fig. 2.12 for Tw = 70°C and Fig. 2.13 for Tw = 25°C show that the interaction pressure is not significant compared with the triggering pressure.

In one experiment with 70°C water, Bang shortened the time for the triggering as he reasoned that the surface of the water had been frozen since the time was too long. With the triggering at 2.5 seconds after the flooding was started, a violent interaction occurred. The front Plexiglas wall of the vessel was destroyed and the

fragments were energetic enough to cause damage to some equipment. The pressure recorded in this case is shown in Fig. 2.14. This confirms the violence of the explosion. It is interesting that the magnitude of the pressure increases as the interaction propagates and there is the second propagating event in the opposite direction resulting in the much larger impulses, which might be the cause of the vessel damage. Three more tests with the same experimental conditions were repeated for further investigation, but none of these reproduced the same degree of the violent interaction, even with the exactly same conditions.

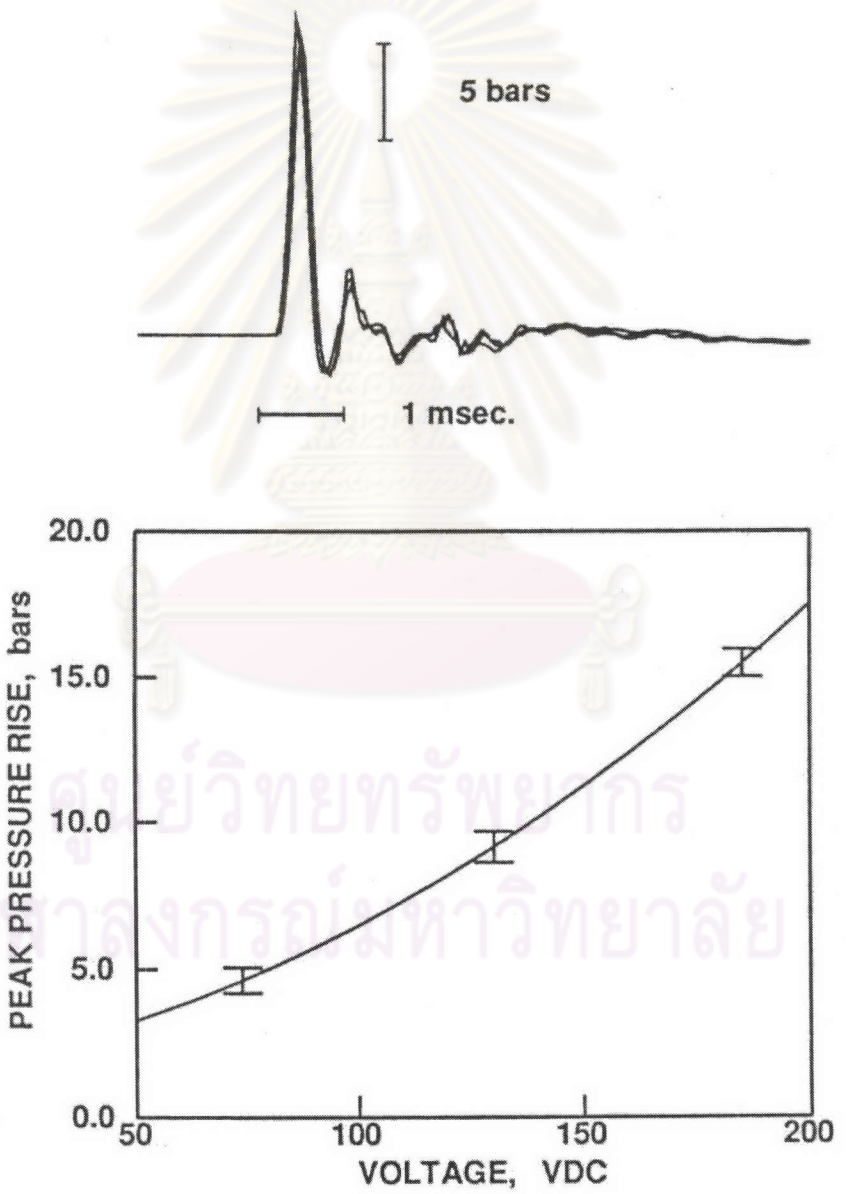

Fig. 2.9 Reproducibility of trigger pressure (top) and trigger pressure peak v.s. capacitor voltage (bottom) [9]

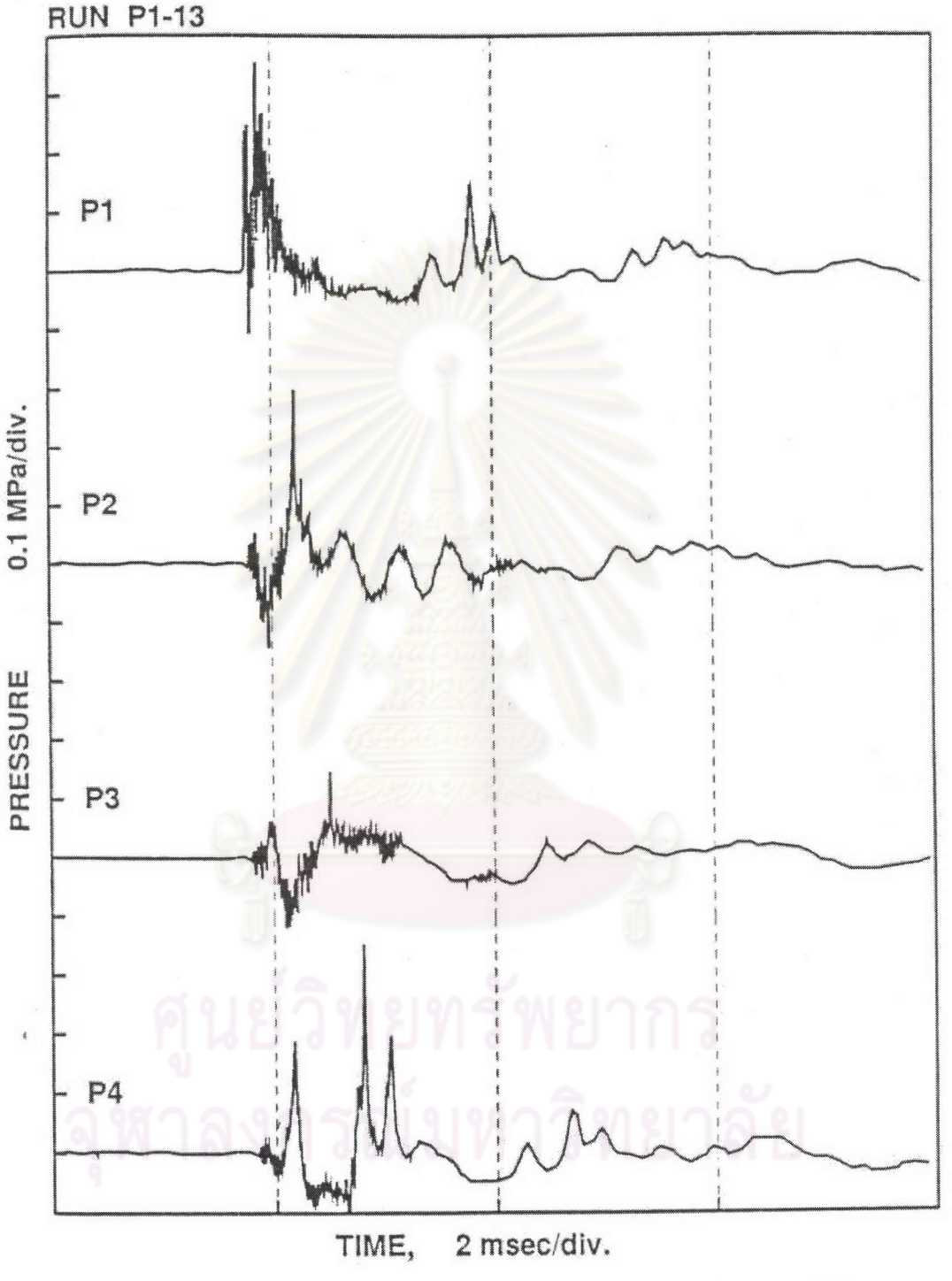

Fig. 2.10 Typical pressure records of trigger pressure in water [9]

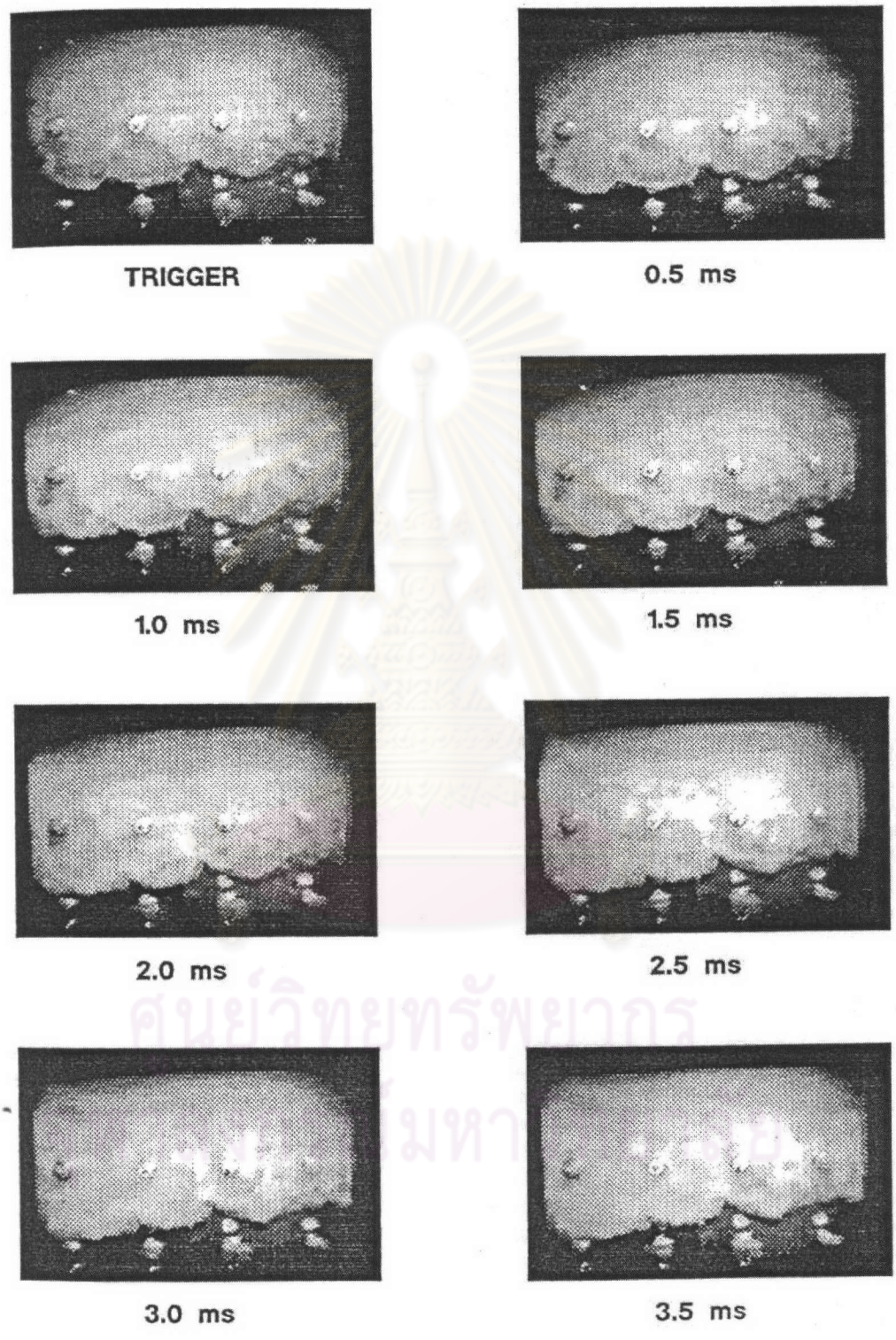

Fig. 2.11 Select frames in high-speed film of water/LN2 interaction [9]

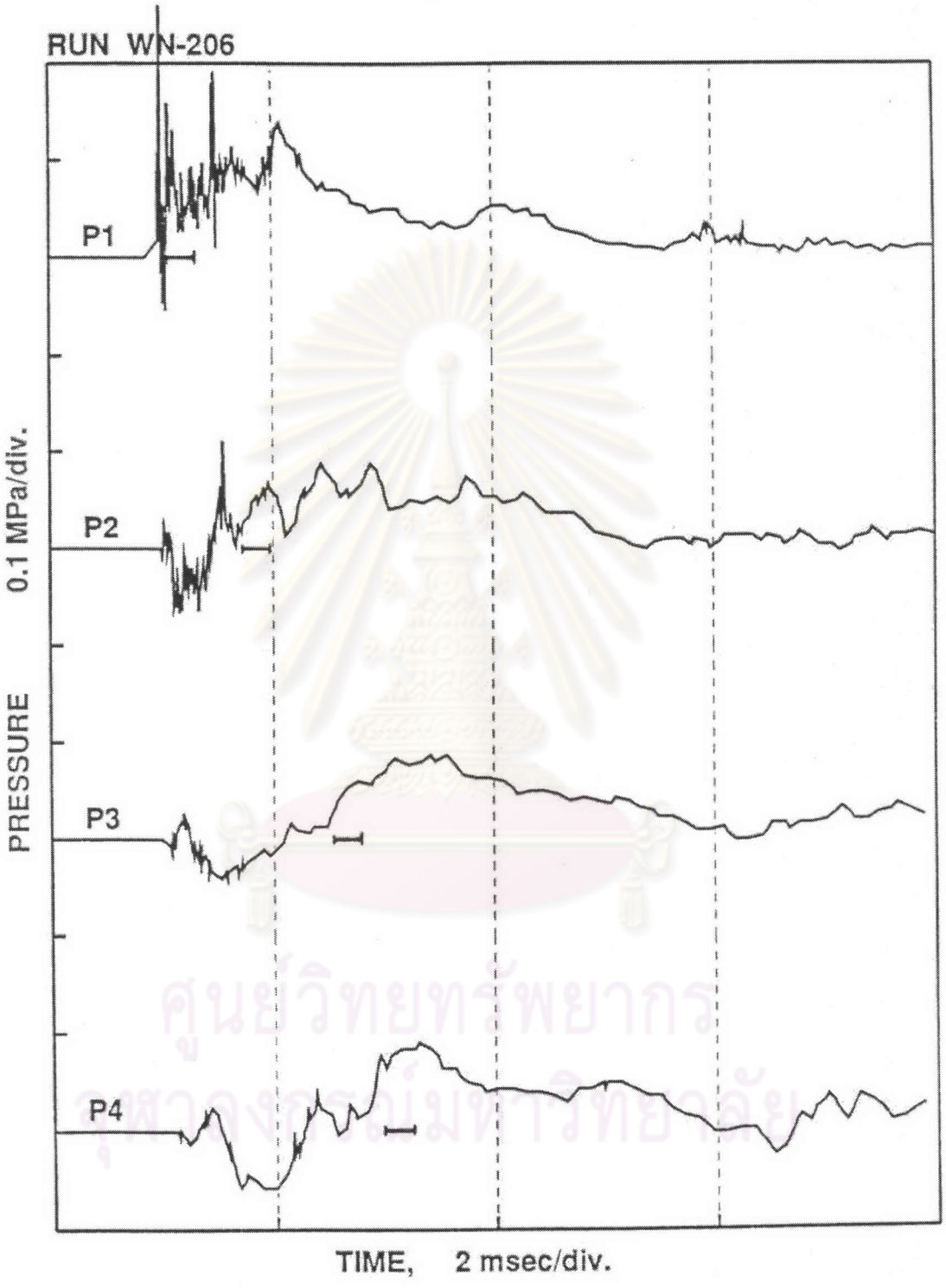

Fig. 2.12 Pressure records in experiment WN- 206 (Tw=70°C) [9]. The interaction pressure shows less significant when compared to the trigger pressure.

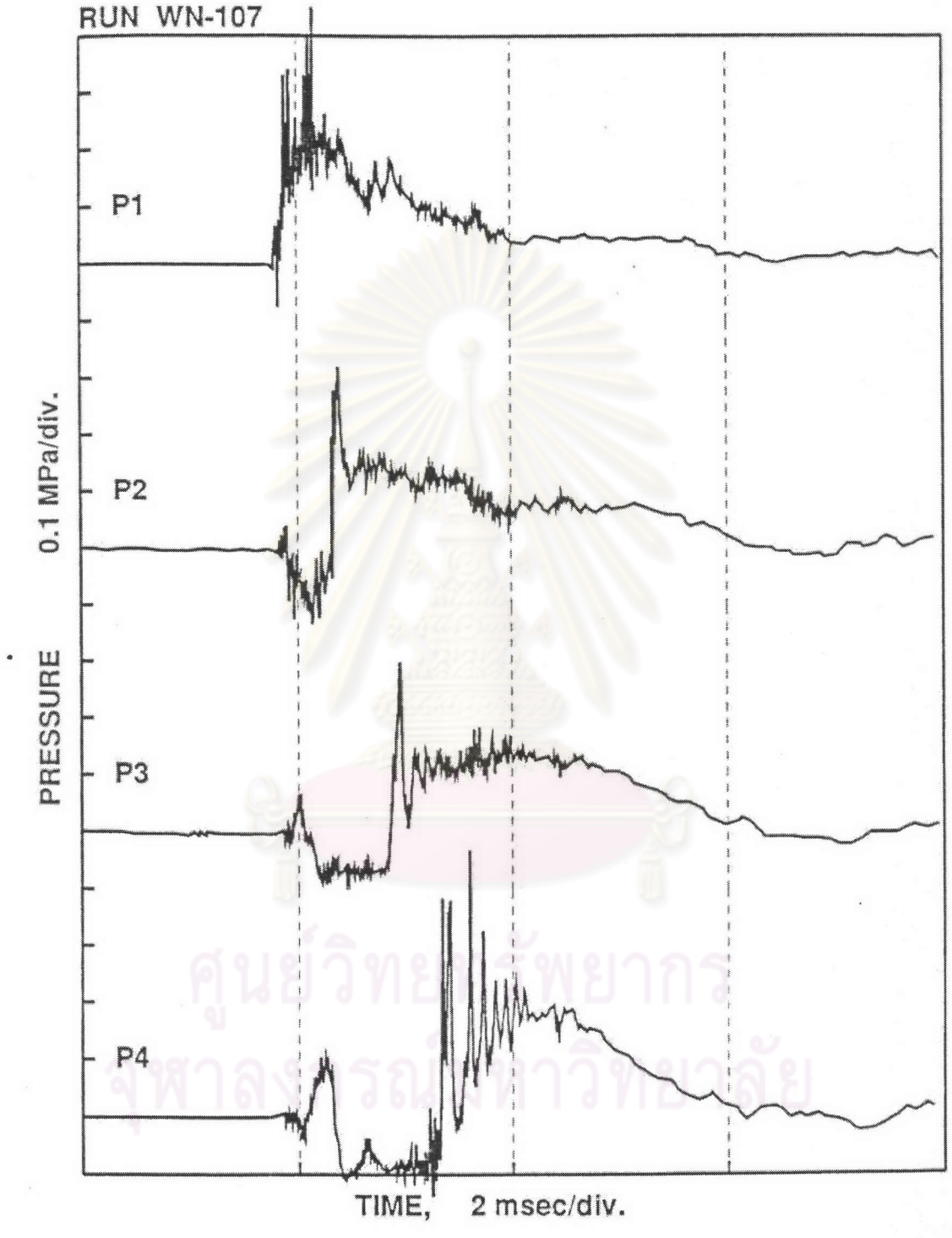

Fig. 2.13 Pressure records in experiment WN-107 (Tw=25°C) [9]. The interaction pressure shows less significant when compared to the trigger pressure.

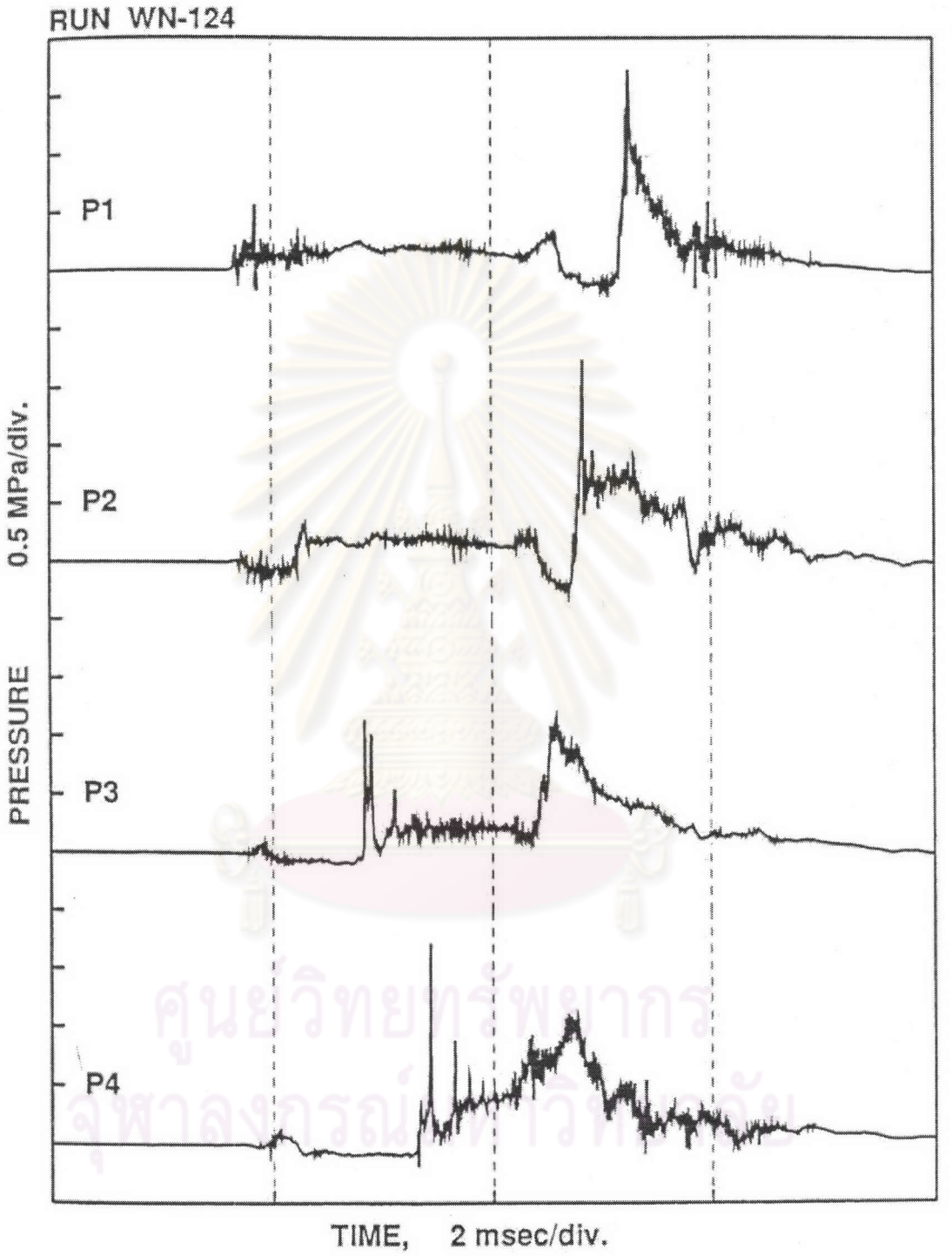

Fig. 2.14 Pressure records in the experiment with violent interaction [9].

The magnitude of the pressure increases as the interaction propagates and there is the second propagating event in the opposite direction resulting in much larger impulses.

Sunchai et al. [12] planned on conducting the experiments on the low temperature vapor explosion. The objective of the experiments was to simulate the interaction between the molten fuel and the volatile cooling liquid without resorting to the high temperature. The experiments involved the injection of the liquid material at a moderate temperature into the liquid material with the very low boiling temperature in order to observe the level of the pressurization as a function of the temperatures and masses of the applied materials. For this purpose, the liquid nitrogen and the water were chosen as the coolant and the injected material in the confined close system for this experiment. The finished installation is shown in Fig.2.15.

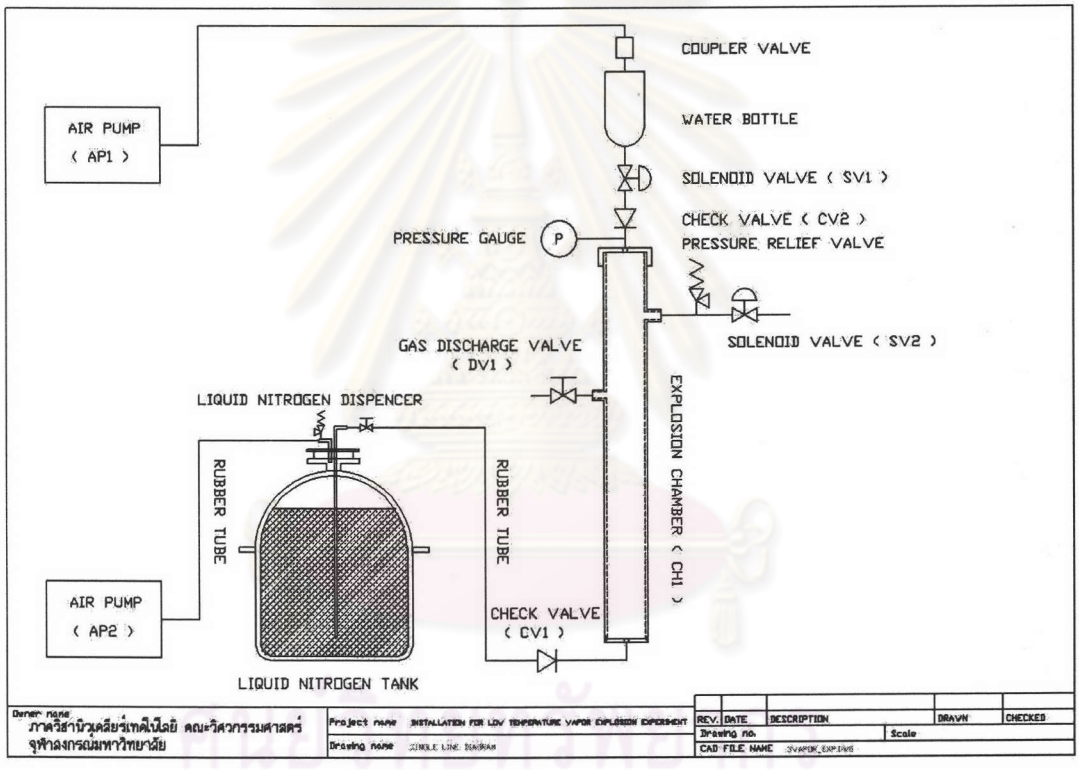

Fig. 2.15 Finished installation for the low temperature vapor explosion [13]

Urith et al. [14] investigated the possibility of the occurrence of the vapor explosion at the condition of the low temperature. They modified the original installation shown in Fig. 2.15 to the new installation shown in Fig. 2.16. In their experiments, the water is simulated as the hot liquid, and the liquid nitrogen is as the colder and more volatile coolant. The experiments were conducted in the room condition by injecting the liquid water into the body of the saturated liquid nitrogen in the close system. It was found that if the water was injected in lump, the pressure

spike was more likely to be observed than when the water was injected in the spray like formation, which was the case observed in the original experiments.

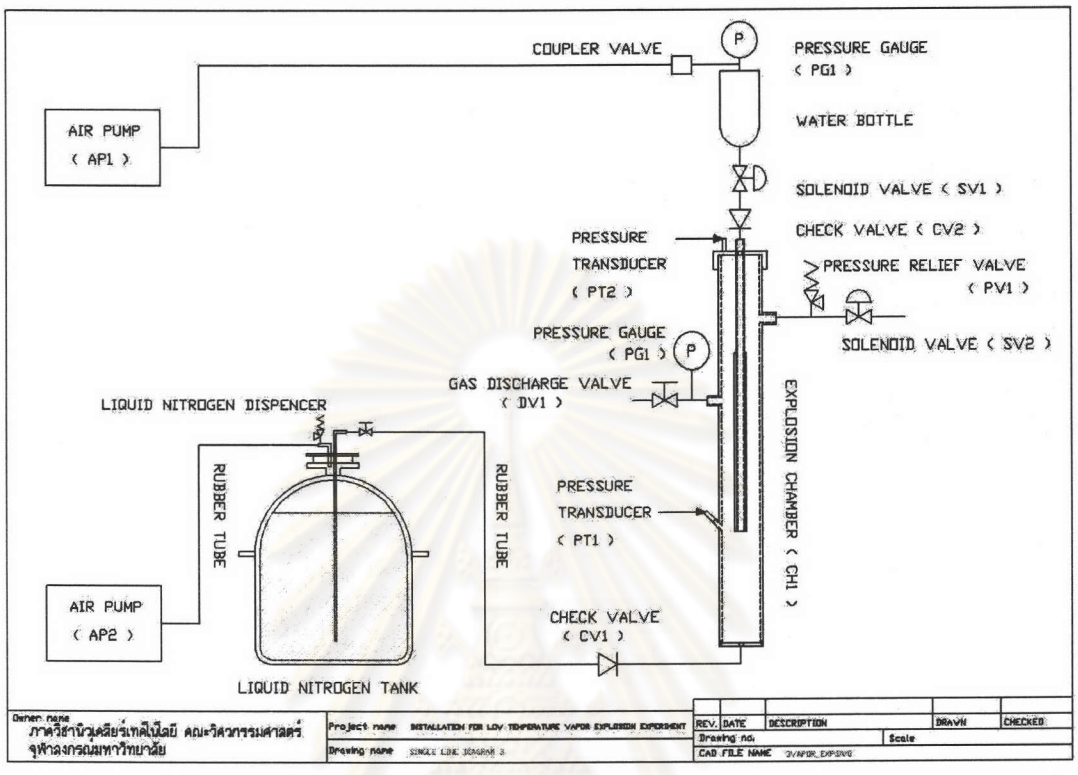

Fig. 2.16 Modified installation for the low temperature vapor explosion [14]

In the potential use of superconducting magnets in the fusion reactor designs, the pressurized cryogenic material such as the liquid helium or nitrogen is used to cool the magnet in the primary loop and the water is used in the pressurized secondary loop. The water could possibly come into contact with the liquid cryogenic. Duckworth et al [5] studied the vapor explosions between water and cryogenic materials, liquid helium and liquid nitrogen. An experimental facility has been built to characterize the interaction between the subcooled, pressurized water and liquid helium or liquid nitrogen. The facility for water and liquid helium is shown in Fig. 2.17.

The initial water temperatures varied between 120°C and 150°C at the pressures between 310 kPa and 520 kPa. The mass of water was from 36 g to 384 g. The initial liquid helium temperature was ~4 K at the near atmospheric pressure. The

volume of the helium was from 3.28 L to 20.8 L and the nozzle diameters varied from 2.0 to 12.0 mm. The test conditions are shown in Fig. 2.18. The pressure profiles during the interaction are shown in Fig. 2.19. One interesting test is the test run#8. The results show the saturation value of the data acquisition system and the maximum dP/dt is 821 kPa/s or 8.21 bar/s.

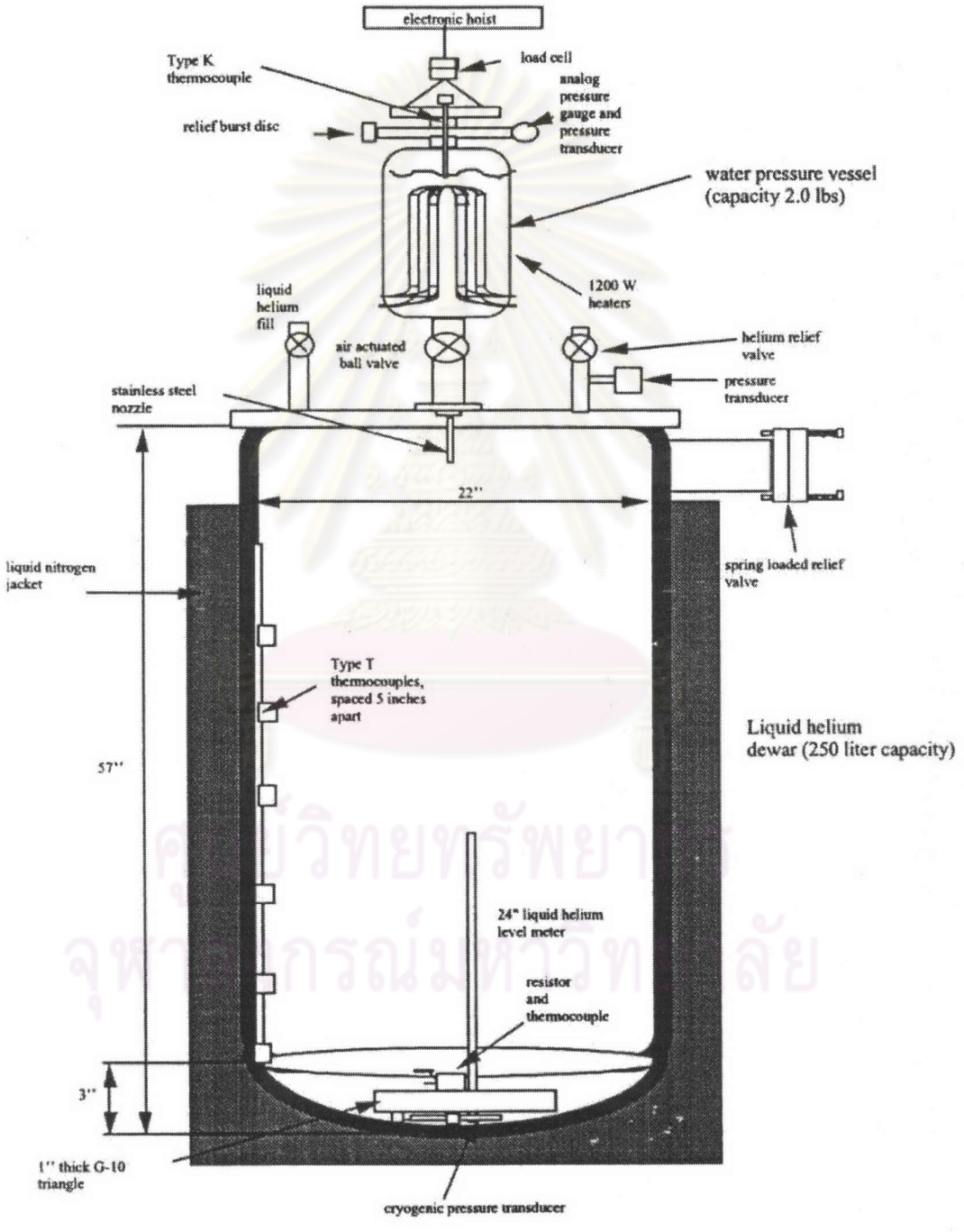

Fig. 2.17 Water - Liquid helium experimental facility [5]

Run	D mm	P_w kPa	T_w C	m_w kg	t s	V_{he} L	dP/dt kPa/s
1	2.0	490	147.0	0.165	0.960	19.8	58.96
2	2.0	352	142.1	0.104	0.500	19.8	29.90
5	2.0	401	134.0	0.067	0.720	20.8	1.471
6	2.0	402	134.1	0.074	0.385	20.8	44.51
7	2.0	317	122.0	0.036	0.480	20.8	1.033
8	12.0	317	122.0	0.384	0.355	7.05	821.9
9	2.0	307	121.8	0.047	0.275	7.05	31.53
10	2.0	307	121.5	0.038	0.255	3.28	1.663
11	2.0	314	121.9	0.073	0.605	3.28	31.03
12	2.0	312	122.8	0.107	0.565	2.22	30.82
13	8.1	320	123.0	0.229	0.295	7.05	527.5
14	5.0	306	120.0	0.152	0.325	5.73	139.7
15	5.0	318	122.1	0.194	0.750	7.05	179.3
16	10.0	300	121.1	0.358	0.430	7.05	790.0
17	10.0	300	121.8	0.289	0.220	7.05	704.4
18	2.0	405	134.0	0.106	0.230	7.05	33.04

Fig. 2.18 Initial conditions and results of water and LHe experiments [5]

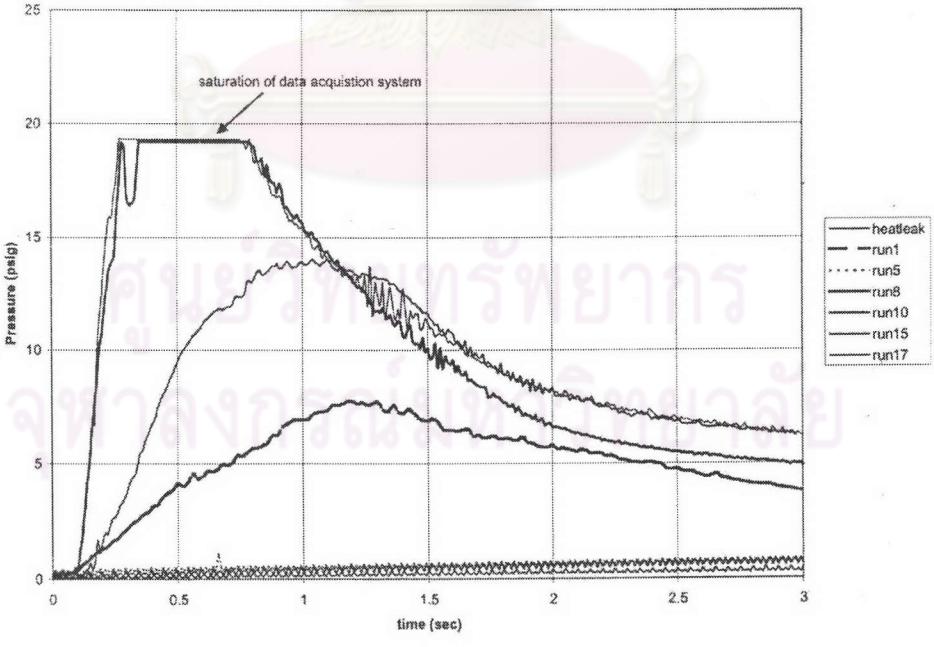

Fig. 2.19 Pressure profiles during the interactions of water and liquid helium [5]

The facility for the water and liquid nitrogen is shown in Fig. 2.20. The results were consistent with that of the water and liquid helium but the pressurization was much less. The pressure profile is shown in Fig. 2.21. The pressurization was 0.206 kPa/s. Duckworth explained that the water and liquid nitrogen experiment had a significantly larger expansion volume than the water and liquid helium experiments.

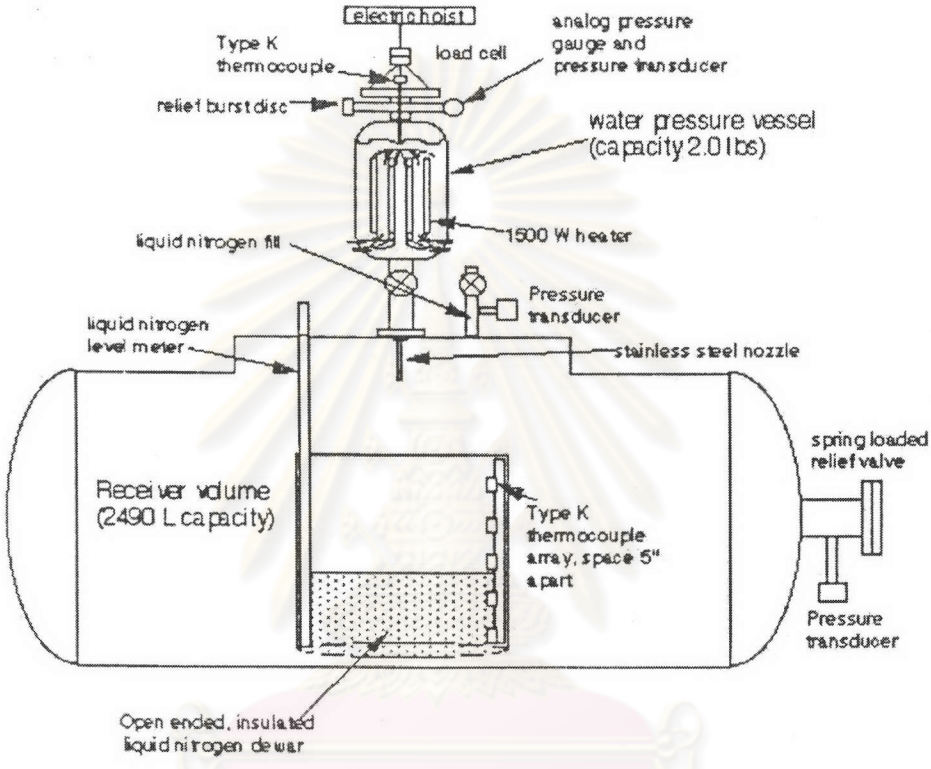

Fig. 2.20 Water and liquid nitrogen interaction experimental facility [5]

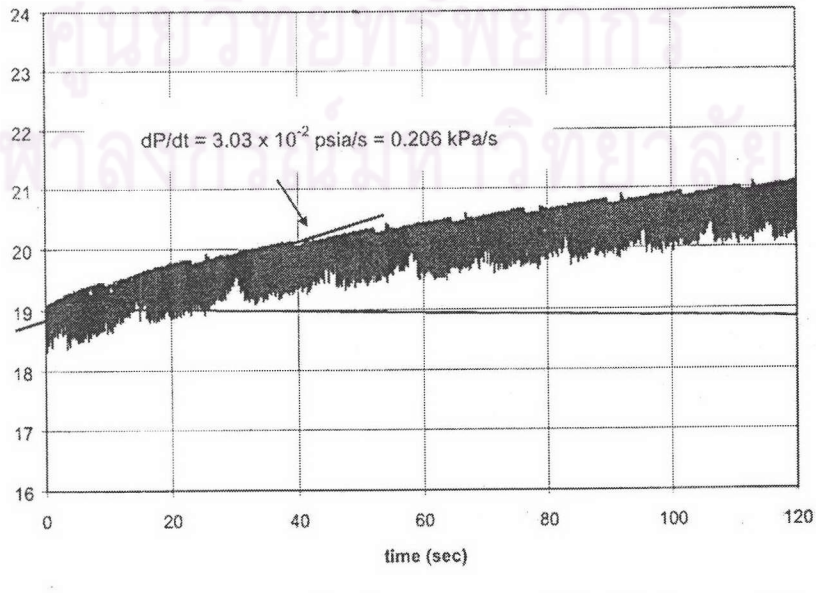

Fig. 2.21 Pressure profile from water and liquid nitrogen [5]

2.4 Small-Scale Experiments

As earlier stated, the objectives of the small-scale experiments are the better understandings the fundamental mechanism of the vapor explosion. By nature the effect from the small-scale experiment is very low when compare to the large-scale experiment. The transparent vessel accompanying with high-speed video camera can be used for the investigation.

An investigation on the mechanisms of fragmentation of the molten metal was performed by Witte et al. [15]. A few grams of a molten (lead, bismuth, or tin) dropped into water in an 8.4 cm ID, 20 cm long quartz tube. They found that the fragmentation of the tin drop was very violent when the initial temperature was above 370°C. The lead did not fragment up to 590°C. And the bismuth fragmented extensively, and became even more extensive as the temperature increased. In some cases, when several molten drops entered the water, the fragmentation of a drop was followed immediately by fragmentation of the other drops. In their experiments, they found that the boiling interaction time was slightly longer period of time than the oscillation time for vapor collapse and reformation around small solid spheres. They thought that the violence caused by collapse and reformation of vapor was not significant since there is insufficient time for its development. In turn they suggested from their experiments that the impact pressure upon vapor collapse, reduction in interfacial surface tension upon liquid-liquid contact, and thermally controlled phenomena such as the superheating of the cold liquid could be the cause of fragmentation.

Dullforce et al. [16] performed over 300 small-scale experiments to investigate the interaction that sometimes occurs when hot liquid metal was poured into a container of water. In these experiments, 12 grams of molten tin were used. The violence of each interaction was classified by measuring the ratio of the mass of comminuted tin to the original mass of tin, and the effect of varying the initial tin and water temperatures, T_f and T_c, was investigated. In T_f - T_c space there was a zone, the temperature interaction zone (TIZ), outside of which the interactions do not occur without the external triggering. The TIZ is shown in Fig. 2.22. The left vertical

boundary of the temperature interaction zone (TIZ) is close to the melting point of tin and the bottom boundary is the freezing point of water. The top sloping boundary indicates that a certain subcooling of cold liquid is required for a self-triggered interaction at a given hot liquid temperature. It was suggested that the vertical and sloping boundaries of the TIZ are dependent on the mass of the hot liquid; the vertical boundary moves to the right and the sloping boundary moves down as the fuel mass is decreased.

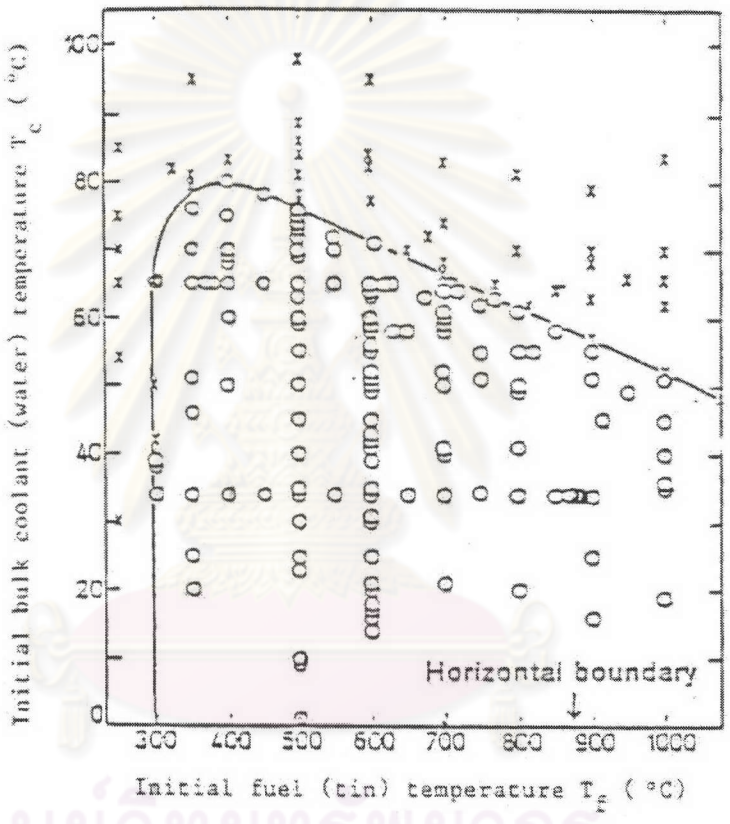

Fig. 2.22 Temperature interaction zone in molten tin drop and water [16]

Zyszkowski [17] performed the thermal interaction experiment between molten copper particles and water. The copper temperatures ranged from the copper melting point to about 1800°C and the water from 15-80°C. The particles dropped and entered the water as shown in Fig. 2.23. The transient temperatures of the copper particles and water before and during the interaction were measured. The history of the phenomena was filmed by means of a high-speed camera (to 8000 fps). According to his proposed hypothesis, the thermal explosion occurred when the molten metal had the temperature of its solidification and the heat transfer on its surface is

sufficiently intensive. The "sharp-change" of the crystalline structure during the solidification of the molten metal is the cause of the explosive fragmentation.

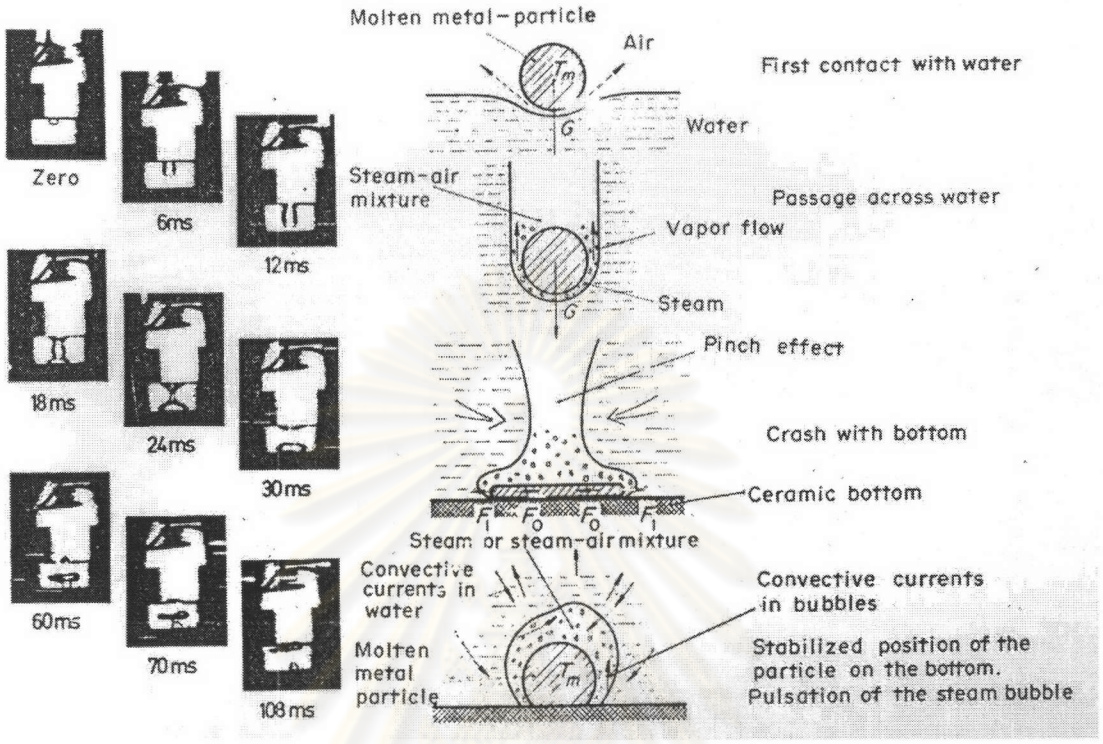

Fig. 2.23 Schematic model of particle-entry in water [17]

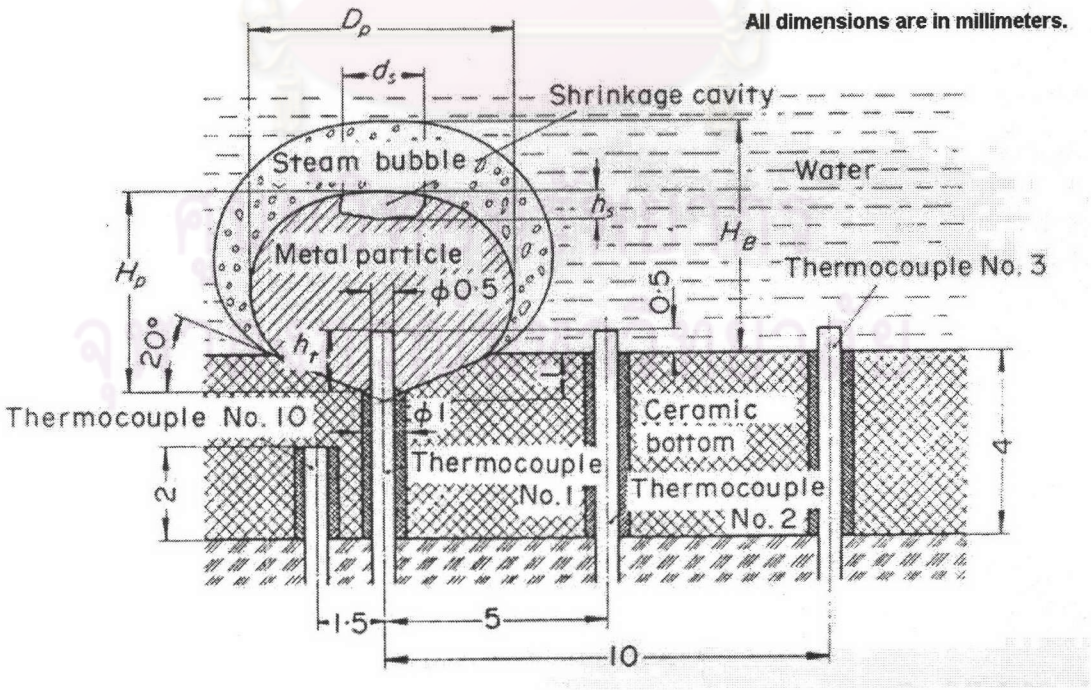

Fig. 2.24 Model of a metal particle on the bottom of the experimental vessel [17]

One of the more informative small-scale experimental series was that conducted by Nelson and Duda [18, 19]. The experiment arrangement is shown in Fig. 2.25. They investigated the interactions between the molten iron oxide drop (typically 2.7 mm diameter, 50 mg mass) and the distilled, degassed water over a wide range of the initial conditions. They demonstrated the excellent reproducibility of the test series. The typical pressure and the bubble diameter history during the explosion of a single drop of iron oxide in water are shown in Fig. 2.26. The bubble grew and collapsed due to the steam produced by the initial contact between the melt and water. They also explained that the bubble over-expanded during its growth and the steam began to condense as it encountered a steadily increasing surface area of cold water. Upon the collapse of the bubble, a pressure transient was generated that acted as another trigger pulse, which again collapsed the film around the melt drops. This caused the fragmentation of more melt and the regrowth of the bubble. These growth-collapse cycles continued to fragment the melt until further breakup could not continue, probably due to the freezing of the melt. The size of fragmented melt debris ranged from 20 μm to 1 mm. It was observed that the interactions were initiated beyond the temperature interaction zone [16] by an external trigger using an exploding wire.

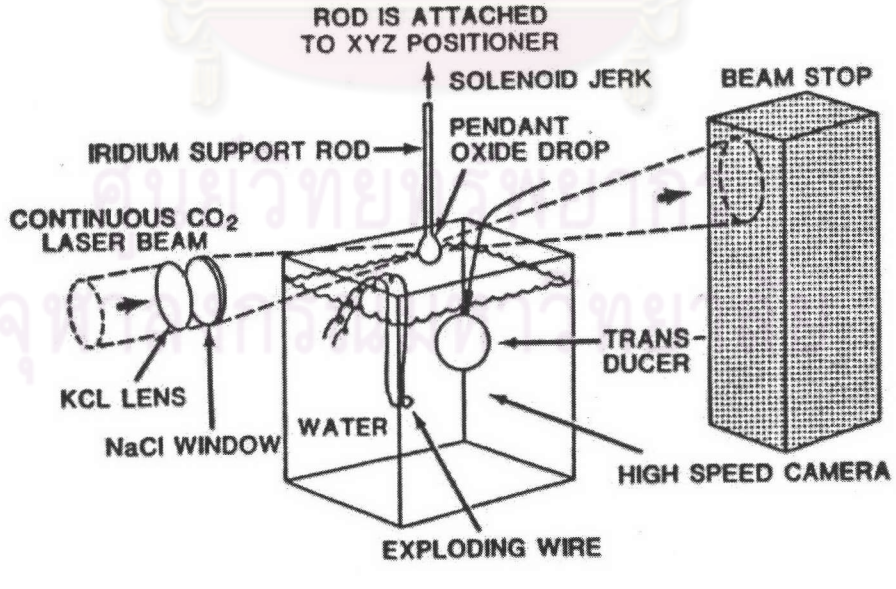

Fig. 2.25 Laser Melting Arrangement [18]

Nelson and Duda also investigated the effect of the fall height of a drop. As the fuel drop fell into the water, air was entrained with the drop as it entered the water in the form of a non-condensible gas bag. The volume of air entrained in the wake behind the drop increased as the fall height increased. If it fell from a certain height, it would not explode spontaneously. If its fall height is lowered, a spontaneous FCI occurred. The air entrainment was suspected as a cause of the suppression of the spontaneous FCI.

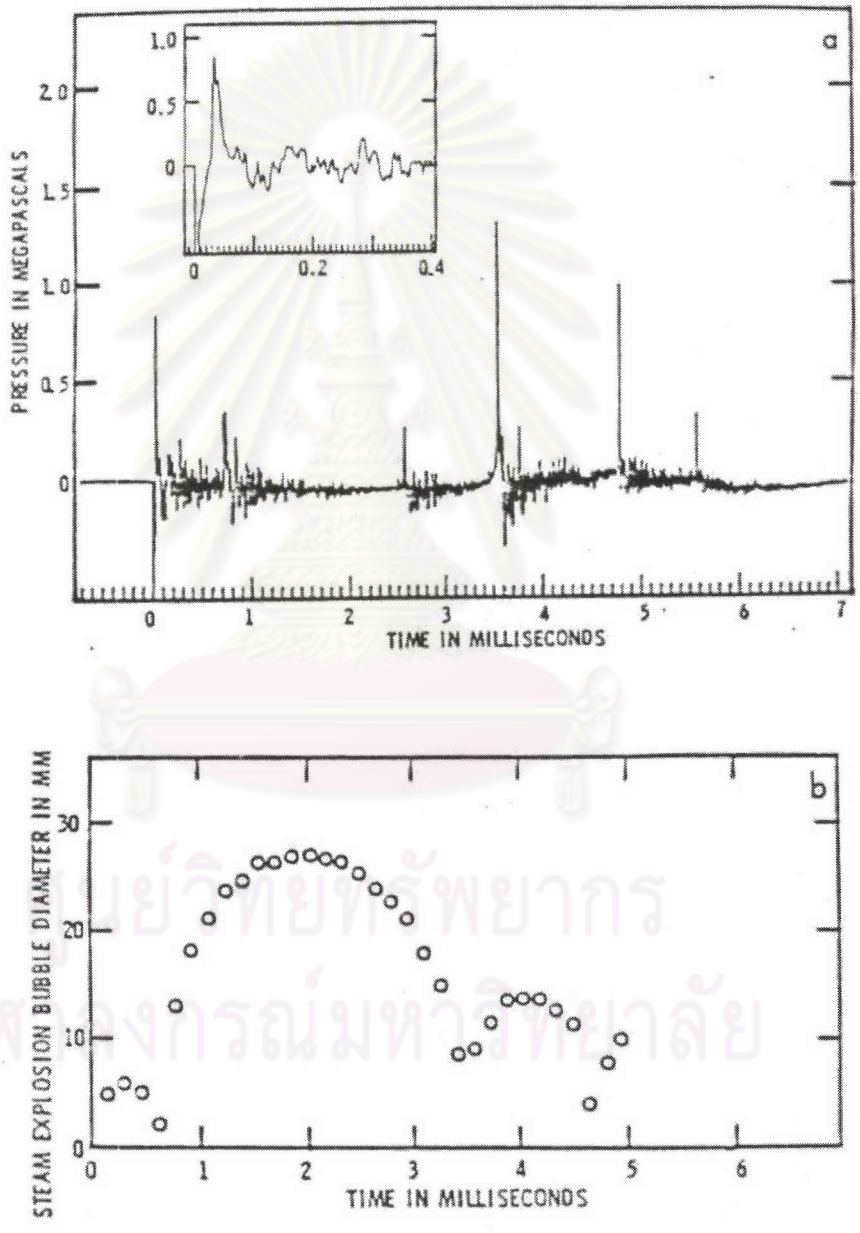

Fig. 2.26 Interaction pressure (top) and bubble diameter (bottom) profiles produced during a single drop of molten iron oxide and water interaction, the bridge wire exploded at time zero [18]

Up to now the small-scale experiments are still being conducted. Yutaka et al [20] studied the trigger mechanism of vapor explosion in 2002. The interaction between a molten droplet and water was recorded with a high-speed video camera with the maximum speed 40,500 fps. The results from the experiments agreed with those from the past experiments. However, they proposed a schematic diagram of the trigger process for the vapor explosion as shown in Fig. 2.25. The film collapse is concluded as a trigger but how the film collapse fragments the liquid is still not exactly known.

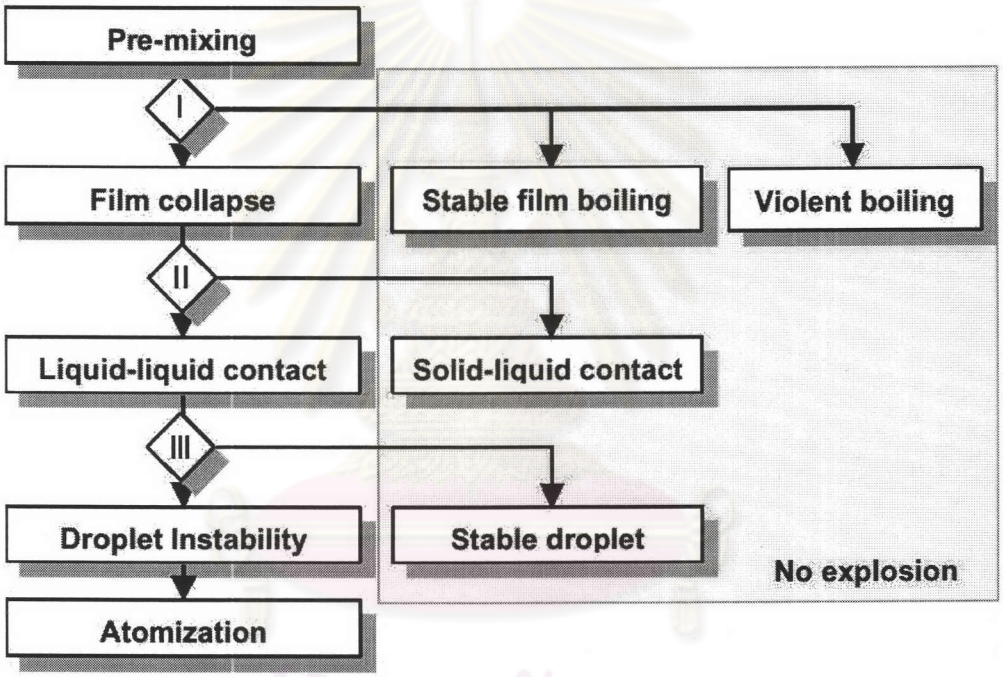

Fig. 2.27 Schematic diagram of trigger process to vapor explosion [20]

Some information of the small-scale experiments can be derived as followed:

1. The delay time or "dwell time" between the initial contact and the interaction exists. It increases systematically with the temperature of both the hot liquid and the cold liquid. This suggests that film boiling destabilization is a cause of the interaction initiation.
2. There is a temperature interaction zone in which violent interaction occurs. The lower cutoff point of the hot liquid temperature is comparable to the spontaneous nucleation temperature of the cold liquid (e.g., 300°C for tin

and water). External trigger causes the violent interaction even below the cutoff point.

3. The fragmentation of the hot liquid is a process that has a major effect on the vapor explosions; the more efficient interaction results in the finer fragmentation and the more violent explosion.
4. If the major portion of fuel is solidified before the vapor film is collapsed, no explosion occurs except in the case of the molten copper in which the thermal stress cracking of the solid crust induces the cavity and causes the molten copper to contact the water.
5. The presence of non-condensible gas suppresses the spontaneous FCI.

2.5 Theory and Modeling

One of the most references in many works up to now is the review of theory and modeling written by Corradini [1]. The theory and modeling, which is described in this dissertation, is an abbreviation of his review but with some updated details.

2.5.1 Mixing

In this phase, the fuel and the coolant interact to each other "quietly" with low pressurization and interpenetrate and mix with each other in a relatively coarse manner. The importance of this mixing process is that the fuel and the coolant remain in this non-explosive metastable state for a dwell time, which allows for the fuel and the coolant to increase the exposed surface area to each other. If this area can be allowed to increase in this quiescent period and still maintain the fuel and the coolant liquid in close proximity, the subsequent explosion could become more efficient. The conceptual pictures of fuel-coolant mixing are shown in Fig. 2.28.

The geometry in Fig. 2.28 does not include the geometry of discrete fuel and coolant liquid masses dispersed in a continuous vapor phase. Two reasons are necessary to be explained:

(1) Such continuous vapor phase geometry implies that the liquid have been fluidized and would not remain in the local mixture region (lack of liquid coolant required for rapid energy conversion), and

(2) this dispersed mixture would be very difficult to pressurize from the fuel-coolant heat transfer during the interaction, because the vapor produced could be relieved from the mixture to the surroundings (the local pressure built-up and the pressure relieved are comparable.)

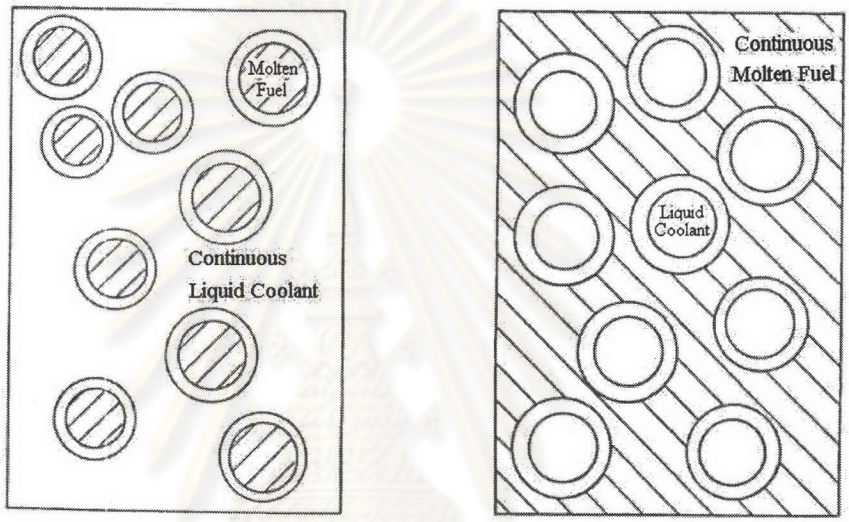

Fig. 2.28 Conceptual pictures of fuel-coolant mixing (a) Fuel within coolant liquid and (b) Coolant within fuel liquid [1]

Henry and Fauske [21] derived an expression to estimate the minimum fuel diameter below which the steam flow would fluidize and drive the coolant out of the mixture. They assumed the heat transferred from the fuel to the coolant must be removed by heat flow from the top of the pool to avoid fluidization. The assumption agrees with the analysis by Corradini et al. [22]. They analyzed from the fully instrumented test series (FITS) experiment performed by Michell et al. [23] and the conceptual picture of the mixture zone is shown in Fig.2.29.

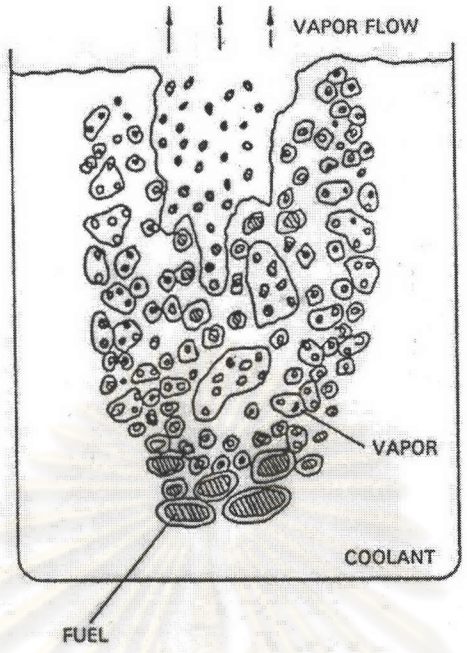

Fig. 2.29 Conceptual picture of fuel coolant mixing as observed in FITS experiment [22]

Theofanous et al [24] addressed the question of a limit for fuel coolant mixing but took a different approach. Instead of investigating the steady-state limit for mixing, they concluded that the mixing process would be driven by the hydrodynamics of transient jet breakup as the fuel pours into a water coolant pool. They also believed that the mixing and breakup might progressively occur. The conceptual picture is shown in Fig. 2.30. Fuel jet mixing regions are in the vertical jet, horizontal jet and vertical rise and fallback. Jet and surface instabilities in each one will produce fuel breakup and mixing. The proposed geometry is the confined geometry, the time available for instabilities to develop is governed by the coolant depth and the jet diameter. Based on their model, if the diameter of a jet is less than 10-20 cm, as for the in-vessel case, it was estimated that Rayleigh jet breakup would lead fuel-coolant mixing. However, if the jet diameter was much greater than 10-20 cm, there was not enough time for the jet to break up into discrete masses due to the Rayleigh mechanism. Therefore, the jet would remain relatively undisturbed and the breakup could only occur at the leading edge of the jet.

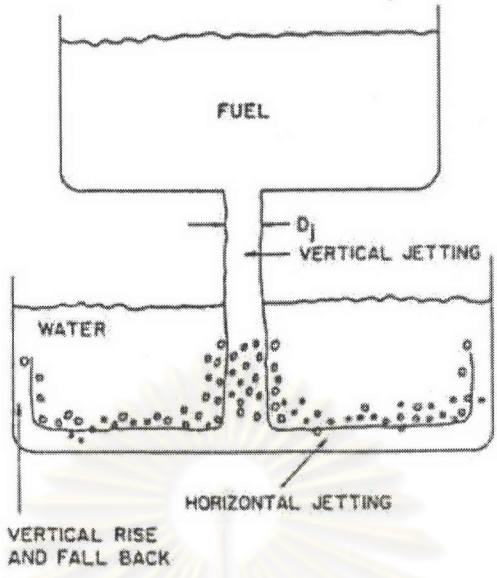

Fig. 2.30 Geometry of fuel pouring into the lower plenum of the vessel [24]

Corradini et al [25] proposed the conceptual pictures of the jet breakup process as shown in Fig.2.31 and 2.32. And these conceptual pictures have been developed into a computer code called **T**hermal **EX**plosion **A**nalysis **S**imulation or TEXAS code. The code simulates the hydrodynamic fragmentation during the mixing and the explosion in the propagation phase. The model can solve the fragmentation in 1-D, three-field equations describing the fuel, coolant vapor and coolant liquid. Two fields represent the coolant as the separate liquid and vapor in an Eulerian control, while the last field models the fuel as the discrete material volumes (or "master particles") in a Lagrangian formulation within the Eulerian region. The conceptual picture of jet fragmentation is shown in Fig. 2.33.

The concept starts with the release of the molten fuel freely as it pours through a vapor region above the water pool. The fuel jet accelerates due to gravity. In this stage the jet remains essentially intact, but small fuel droplets can be stripped off the jet surface due to the relative velocity between the jet and vapor from fluid instabilities. The jet diameter gradually becomes smaller due to the increased velocity and the fuel melt stripping process.

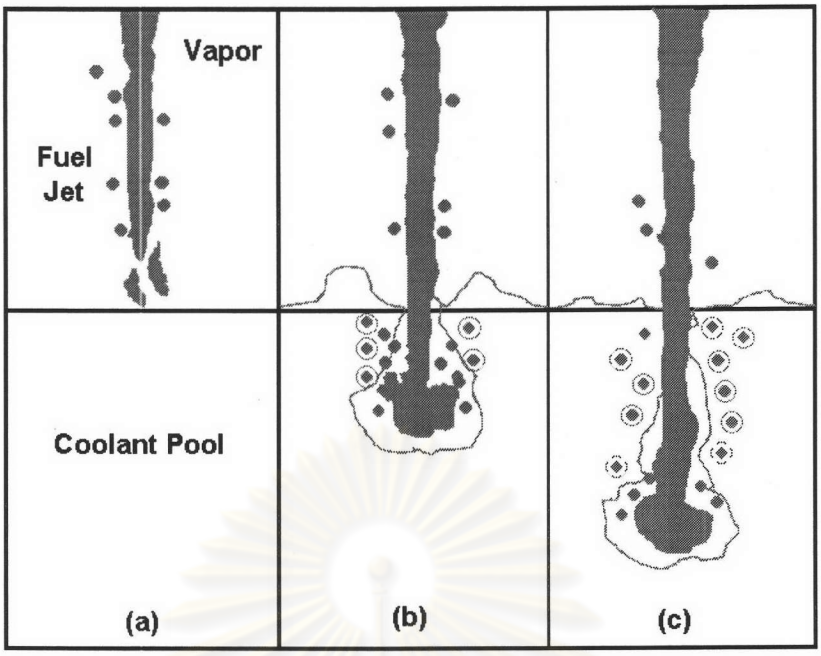

Fig. 2.31: Conceptual Picture of the Jet Breakup Process [25]

(a) Fuel jet breakups in vapor phase region

(b) Fuel jet leading edge grows due to stagnation flow

(c) Fuel jet breakups at leading edge and along jet body

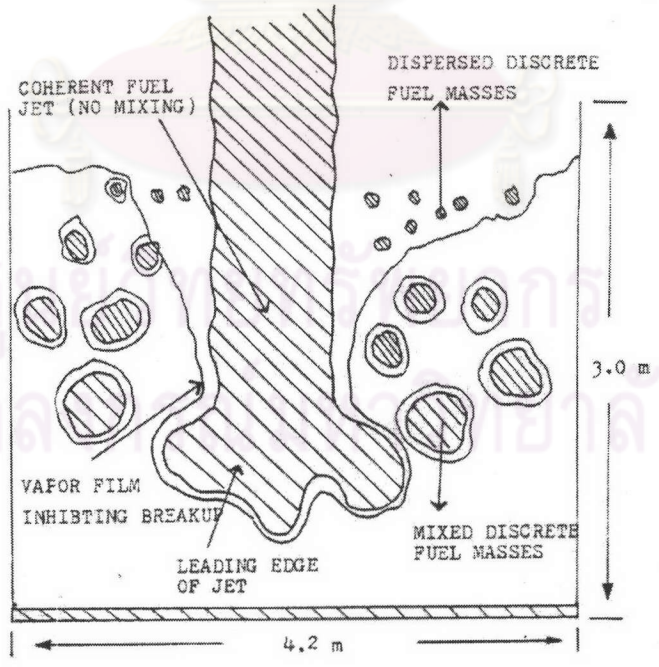

Fig. 2.32 Conceptual picture of fuel jet into coolant pool [1]

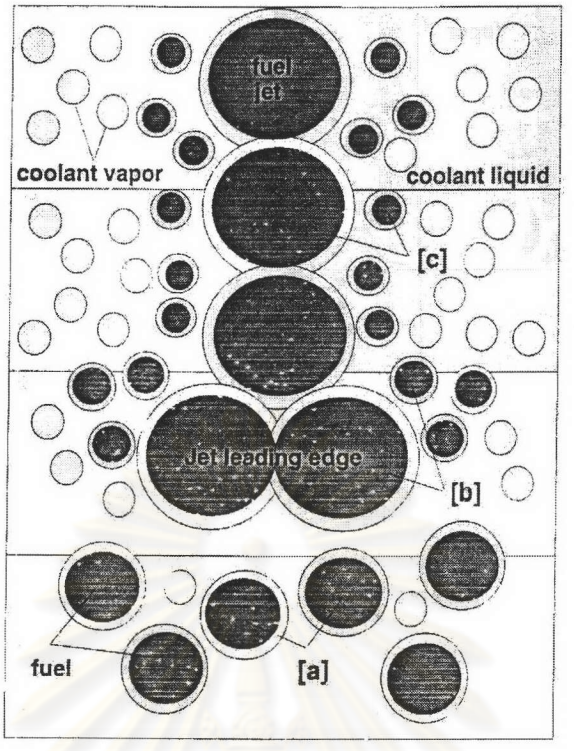

Fig. 2.33 Conceptual picture of current TEXAS mixing model [25]

Once the jet impacts and enters the water pool, its leading edge velocity suddenly slows down. This leading edge experiences the increased drag, the combined dynamic pressure and the shear force exerted by the water. This force causes the jet stagnation flow at the leading edge from boundary layer of the melt. This deforms the leading edge into a "mushroom like" shape as the jet penetrates further. The boundary layer of the melt flows from the front to the rear of the leading edge and is stripped off the jet. The boundary layer stripping (BLS) is assumed to be the dominant mechanism that explains the melt leading edge breakup behavior. As the jet continues to penetrate the water pool, the unstable wave will grow along the surface of the jet column above the leading edge due to the Kelvin-hemlholtz instability (KHI). A good example of KHI can be seen on the surface of a lake when the wind blows over it, leaving unstable ripples or waves behind. The amplitude of the unstable wave grows fast enough and overcomes the fuel surface tension and the dynamic pressure surrounding its peak. The melt droplets are finally detached from the peak, which escalates the breakup of the jet column. If the relative velocity is

large, the sizes of the stripped melt droplets will be small; possibly less than 1 mm. In addition, to these short wave instabilities or KHI, long wave instabilities also exist, comparable to the melt jet diameter. The growth of these instabilities leads to the breakup of the jet column into large discrete "lumps". For these melt "lumps", in particular, as well as for the other fragmented fuel mentioned before, further breakup would occur due to Rayleigh-Taylor instabilities (RTI) until the discrete melt masses reach a stable size indicated by their Weber numbers. If the coolant pool is deep enough, this process will continue until the jet is completely fragmented into the stable size debris as it mixes and settles in the coolant pool.

Each of the three hydrodynamic instabilities applied in TEXAS code is considered to be dominant at the specific location of the jet surface. In Fig. 2.33, the jet is composed of three parts (1) leading edge of the coherent jet, (2) upper section of the coherent jet above the leading edge, and (3) discrete pieces of the jet below or near the leading edge. BLS is applied at the leading edge, KHI causes the jet surface erosion and drop formation, and RTI breakup of the large wave instability further fragments the discrete melt masses from the already broken up pieces of the jet.

The effect of BLS primarily occurs at the leading edge, where the dynamic pressure and shear forces combine to cause a jet stagnation flow at the jet leading edge and to form a surface layer of melt that flows from the front to the rear and is stripped off the jet leading edge. The conceptual picture of BLS is shown in Fig. 2.34.

The effect of KHI is considered to be dominant upstream of the leading edge along the body of the jet, where unstable waves develop due to relative velocity and eventually breakup as droplets shed from the jet surface. The conceptual picture of KHI is shown in Fig. 2.35.

Finally, the main jet body will breakup into large discrete "blobs" due to the RTI. It is very difficult to superpose this RTI mechanism on the jet in the way similar to the other processes. It requires one to track the overall jet shape and continually compute when the jet body pinches off into the discrete lumps due to the larger instability. Thus, the approach or the simplification in TEXAS consider its presence at the start of the pouring process with some initial discrete "blobs" (a given number of

discrete master particles separated from the jet, NBREAK≥1) and neglect it from the coherent jet. Note that the RTI process dominates the breakup of these discrete masses into smaller sizes as well as it does with all the other discrete masses once separated from the coherent jet body by KHI and BLS process.

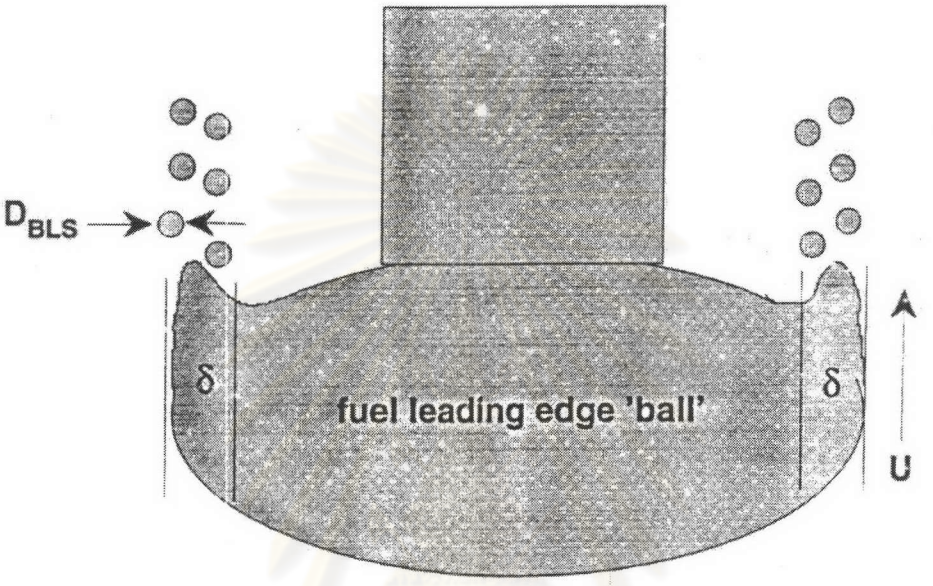

Fig. 2.34 Boundary layer stripping conceptual picture [25]

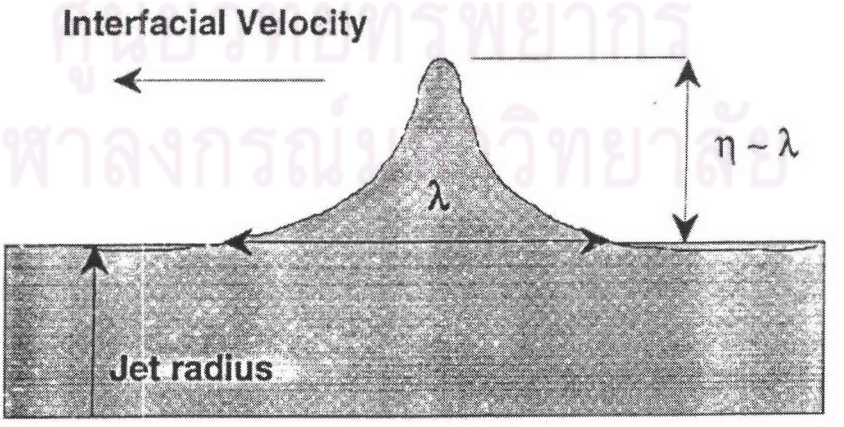

Fig. 2.35 Kelvin-Helmholtz instability wavelet growth [25]

Due to the dynamics effects from BLS, KHI, and RTI, there are always two competing forces [26]: the surface tension and the external inertial force. The surface tension arises from the fact that the molecules in the surface of a liquid are attracted into the body of the liquid by the molecules in the body [27]. Thus, the surface tension tends to maintain its original shape. On the other hand the external inertial force exerted by the flow over the liquid shape tends to induce an inertial force and break the liquid shape apart.

Bohr and Weber introduced a dimensionless number to address the competing forces. The number which is called the Weber number is defined as the ratio of the inertial force ($\rho_c U_{rel}^2$) to the surface tension (σ_f / D_f), and is expressed below.

$$W_e = \frac{\rho_c U_{rel}^2 D_f}{\sigma_f} \tag{2.1}$$

where W_e = Weber number

ρ_c = density of the liquid coolant

U_{rel} = relative velocity between the liquid coolant and the molten fuel

σ_f = surface tension coefficient of the molten fuel

D_f = characteristic dimension of the molten fuel

This dimensionless number includes all the initial causes of the jet breakup. It combines the fuel property, the coolant property, motion and geometry in the form of the fuel surface tension coefficient, the coolant density, the relative velocity and the characteristic length of the fuel, respectively.

Based on the relation between the Weber number and the jet breakup mechanisms, if we increase the relative velocity before both liquids coming into contact, the rate at which the jet is broken up is expected to be also increased. The jet breakup increases the interaction and causes more energetic vapor explosion.

In 1978, Cronenberg [28] performed some experiments to study the relations between the Weber number and the fuel drop fragmentation. Many molten metals were used such as mercury, lead, bismuth and tin. The results showed that the fragmentation was increased with the increasing Weber number. The plot of Weber number versus number of fragments for molten metals dropped in room-temperature water as shown in Fig. 2.36.

During the mixing, by jet breakup mechanisms described above, the coolant begins to be vaporized at the fuel-coolant interface. This creates the vapor film that separates the two liquids.

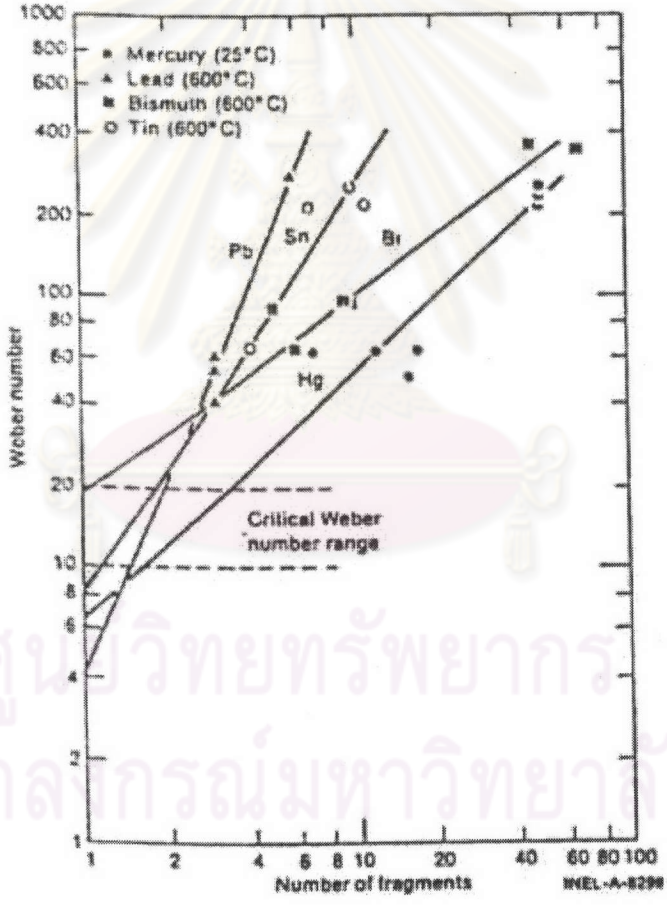

Fig. 2.36 Plot of Weber number versus number of fragments for molten metals dropped in room-temperature water [28]

2.5.2 Triggering and Local Fuel Fragmentation Phase

The model for how the film collapse fragments the fuel was proposed by Kim [29]. He studied the modeling of the small-scale fuel-coolant interactions based on the experiments performed by Nelson and Duda [18,19]. The modeling of the small-scale single droplet fuel-coolant interactions was conceptually divided into four phases as shown in Fig. 2.37 and the last three of which could occur cyclically:

1. Film boiling around a molten fuel droplet in coolant;
2. Film collapse due to an external pressure pulse and coolant jet formation due to Rayleigh-Taylor instability in a spherical geometry;
3. Jet penetration into the molten fuel and encapsulation in the fuel;
4. Expansion of the molten fuel surface due to the rapid evaporation of the encapsulated coolant and fragmentation of this fuel surface.

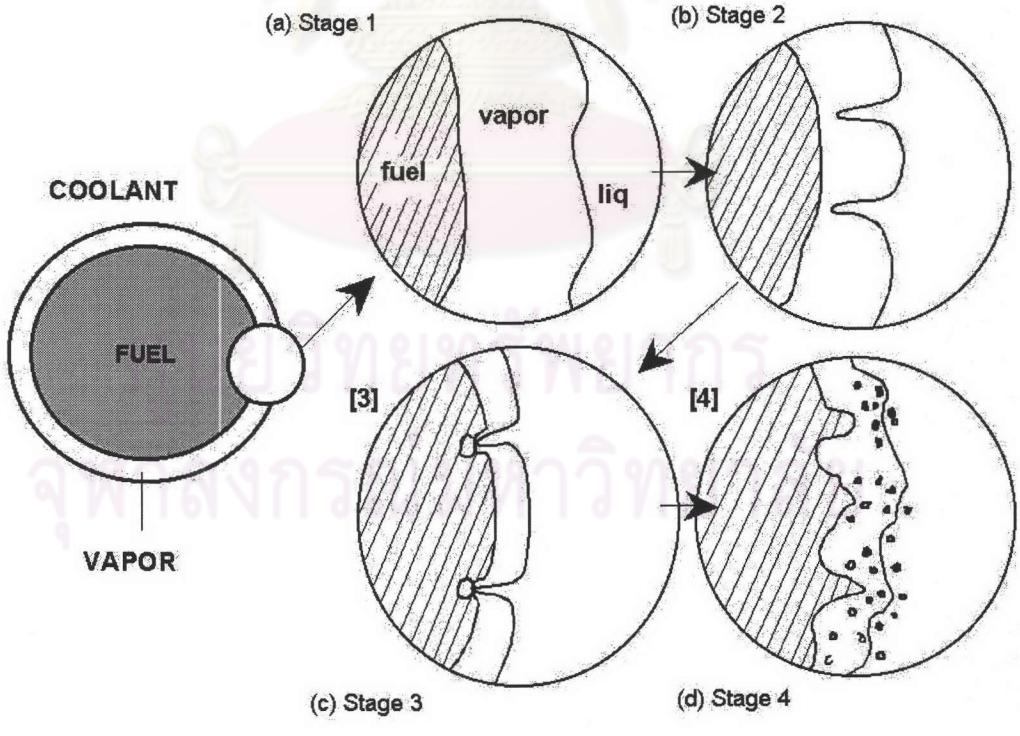

Fig. 2.37: Kim conceptual model in the triggering phase [29]

In this triggering phase, Corradini [1] claimed that the vapor film is unstable due to its own boiling disturbance or an external pressure pulse. The boiling disturbance causes the film to oscillate especially when the boiling process is between the nucleate and the stable film boiling regimes. With the large enough kinetic energy, the oscillation directly causes the film to collapse. This triggering is called the spontaneous triggering.

Other than the spontaneous triggering, the external triggering by the external pressure pulse is also possible. This kind of disturbance generates the pressure and induces the Rayleigh-Taylor instability, which causes the film to collapse.

As the vapor film collapses, the vapor-coolant interface becomes unstable. The instability, which has a large kinetic energy, forms the minuscule coolant jets. The jet is accelerated and penetrates the molten fuel surface.

The encapsulated coolant drops can penetrate deep into the fuel. The heat transfer vaporizes these coolant drops rapidly and creates the bubbles. These bubbles are expanded under the fuel surface as the local pressure inside each bubble is increased. The bubbles coalesce with the neighboring vapor bubbles and separate the outer portion of the molten fuel surface from the parent fuel droplet. This leads to the outer surface breakup.

However, the coolant drops, which are trapped close to the surface, also undergo the high heat transfer. The heat vaporizes the drops. The vapor expands very fast and drives the thin outer surface breakup without the coalescing of the bubbles.

The expansion velocity induces the multiphase flow of the vapor and the breakup fuel, or the fragmented fuel. The low-density vapor flows with the different velocity compared to that of the high density fragmented fuel.

2.5.3 Explosion Propagation Phase

The heat is transferred rapidly from the molten fuel to the encapsulated coolant with the time scale for the heat transfer that is less than the time scale for the pressure wave propagation and expansion in this local region of the interaction. Therefore, the rise in the local pressure forms a shock wave, which spatially propagates at the speed of sound in the mixture. This is called the explosion propagation phase.

Board et al. [30] suggested a theoretical model in the propagation phase by applying the classical theory for a steady-state one-dimensional chemical detonation to the case of a plane explosion or shock front propagating through a coarsely mixed region of hot and cold liquids.

The shock wave represents a discontinuity of thermodynamic and physical properties as internal energy, entropy, flow velocity, and so forth. A simplified one-dimensional flow with a normal shock wave is shown in Fig. 2.38. The thickness of the shock is usually on the order of a few molecular mean free paths. Ahead of the shock wave the flow is supersonic, whereas behind the shock wave, the flow is subsonic. The temperature, pressure, and density increase across the shock. The flow field to the left of the shock is characterized by the flow velocity u_1, temperature T_1, pressure P_1, density ρ_1 and internal energy i_1. The properties across the shock change to u_2, T_2, P_2, ρ_2 and i_2

Assuming one-dimensional, steady flow, and adiabatic process to the rectangular control volume, the basic equations can be written [31]:

Mass conservation:

$$\rho_1 \cdot u_1 = \rho_2 \cdot u_2 \tag{2.2}$$

Momentum conservation:

$$p_1 + \rho_1 \cdot u_1^2 = p_2 + \rho_2 \cdot u_2^2 \tag{2.3}$$

Energy conservation:

$$h_1 + \frac{u_1^2}{2} = h_2 + \frac{u_2^2}{2} \tag{2.4}$$

and entropy:

$$s_2 > s_1 \tag{2.5}$$

where s_1 = specific entropy ahead of the shock front.

s_2 = specific entropy behind the shock front

Combining Eq. (2.2) and (2.3), and eliminating u_2 yields:

$$\frac{u_1}{v_1} = \left(\frac{p_2 - p_1}{v_1 - v_2} \right)^{\frac{1}{2}}, \tag{2.6}$$

where v_1 = specific volume ahead of the shock front.

v_2 = specific volume behind the shock front

Combining Eq. (2.2), (2.3) and (2.4) and eliminating u_1 and u_2 yields

$$\frac{1}{2}(P_2 - P_1)(v_1 + v_2) = h_1 - h_2 \tag{2.7}$$

where h_1 = enthalpy ahead of the shock front

h_2 = enthalpy behind the shock front.

Board et al. proposed that the complete collapse of vapor blanketing the hot liquid and the fragmentation due to Kelvin-Helmholtz instability and boundary layer stripping will occur because of the differing velocities between the hot and the cold liquid as the shock wave passes.

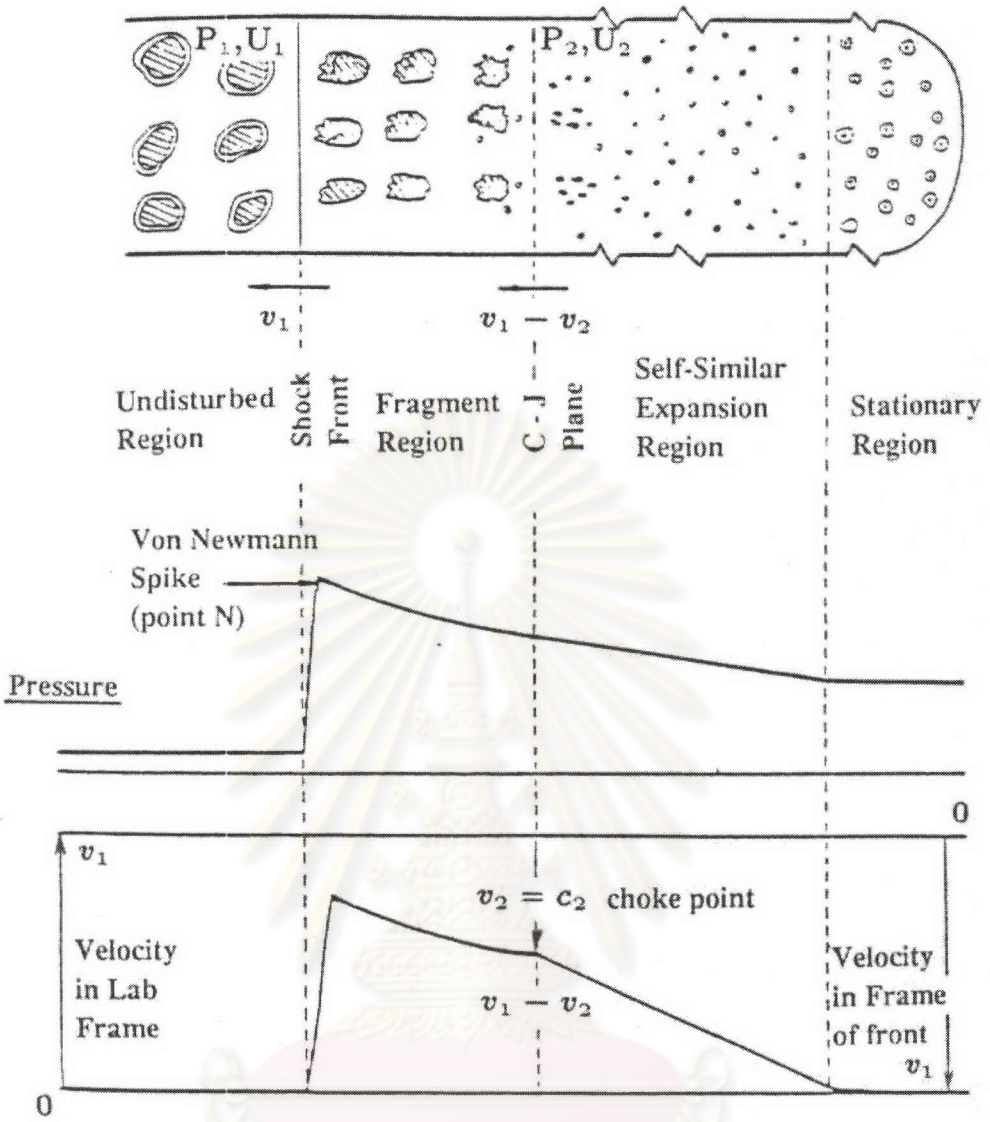

Fig. 2.38 Conceptual illustration of thermal detonation model [30]

2.5.4 Expansion Phase

Immediately after the propagation, the explosion pressure expands and causes the work done on the surroundings which is called the expansion phase. One important parameter in this phase is the conversion ratio. The conversion ratio is the ratio of the mechanical work output produced as a result of an explosion to the total thermal energy of the fuel.

Unfortunately, there was no direct means to measure the work output in most experiment tests [32]. The actual work output can be estimated in the form of the kinetic energy delivered from impulse pressure to the fuel and coolant mixture. This

method has an assumption of a uniform impulse with a defined duration. The other method uses the pressure rise in the FCI system as a result of the explosion. The pressure rise compresses the existing air above the coolant level.

2.6 Some Physics of Ice and Its Solidification

The phase diagram of ice is shown in Fig. 2.39. The broken lines represent the presumed phase boundaries, which have not yet been fully investigated. Dotted lines represent the metastable continuations of one phase into a neighboring region. The ice I structure is tetrahedral co-ordination and the crinkled sheets normal to the c-axis. With the phase diagram, the water and liquid nitrogen interaction is supposed to freeze the water in the region of ice I.

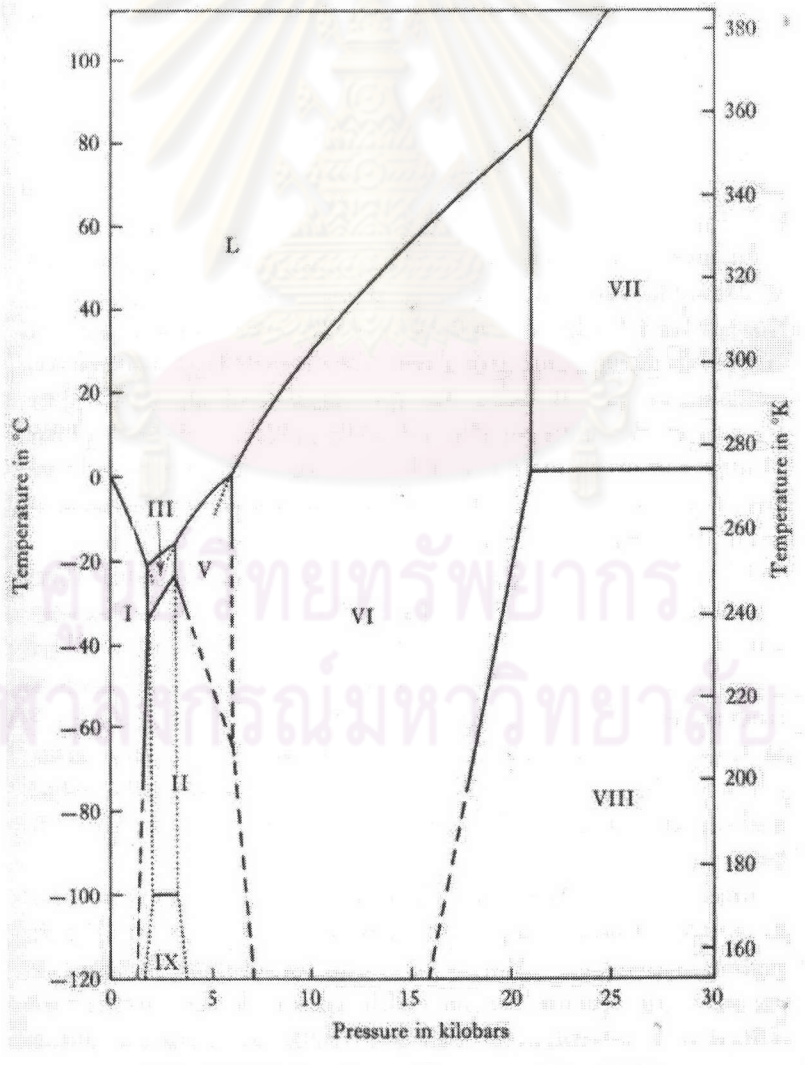

Fig. 2.39 The phase diagram of ice [33].

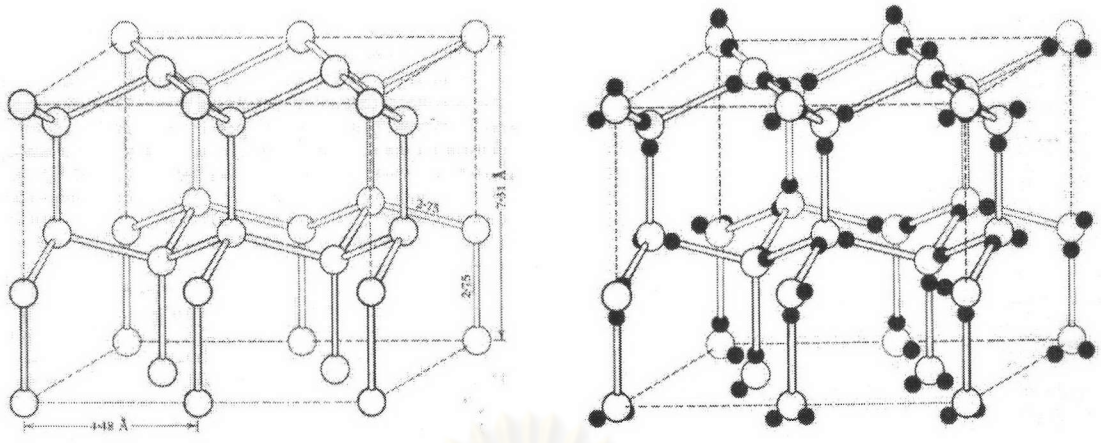

Fig. 2.40 The ice I structure at the temperature of 77 K [33]. (a) Expanded view of oxygen atom positions. (b) A typical disordered arrangement of protons.

Gas is normally dissolved in water. Hindmarsh et al. [34] observed the temperature transition of a suspended freezing water droplet. The schematic diagram of the experiment is shown in Fig. 2.41. and the temperature transition is shown in Fig. 2.42. They also recorded the visible changes during the droplet freezing. The significant changes at the time in Fig. 2.42 are shown in Fig. 2.43. At the point of nucleation, the droplet appears to instantly change from clear to opaque (Frames (A) and (B)). Their video recorder frame rate of 25 per second was not fast enough to record this transition. The next significant change was the appearance of gas bubbles. In Frame (C) these can be seen just below the tip of the thermocouple. As the droplet continues to freeze the number of bubbles increases and after a period of time a bulge appears at the top of the droplet (Frame (D)). In Frame (E) the bulge has grown until it bursts and liquid flows onto the surface of the droplet. The surface liquid freezes and the final droplet shape is formed by the time of Frame (F). No more changes are observable for the remaining temperature transition of the droplet.

The bubbles occurred in the droplet are explained with the fact that air has a much lower solubility in ice than in water so, as ice forms, it rejects the excess gas into the unfrozen liquid. This increase the concentration of dissolved gas in the water until the water becomes supersaturated with dissolved gas. Bubbles will then start to form on the surface of the ice. Due to surface tension and curvature effects, the presence of the bubbles at the solid/liquid interface depresses the freezing point of the water.

It was evident by the fact that the gas bubbles only appeared at approximately the center of the droplet, whereas no bubbles appeared in the outer part of the droplet. It is therefore presumed that the outer part of the droplet froze first and released part of its dissolved gas into an unfrozen center.

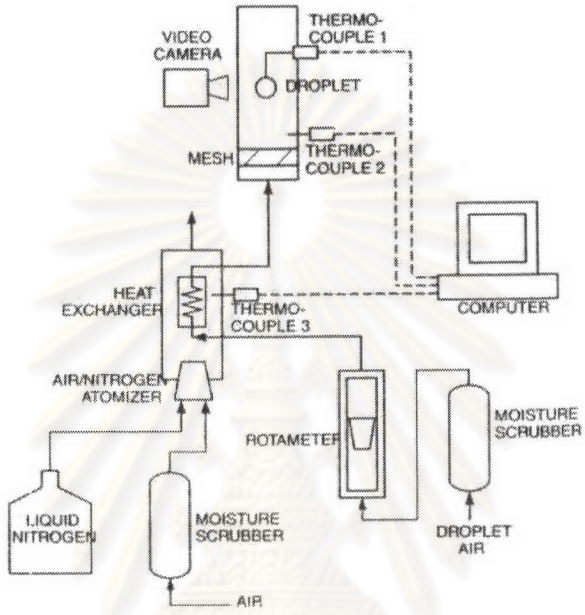

Fig. 2.41 Diagram for the suspended freezing water droplet experiment [34]

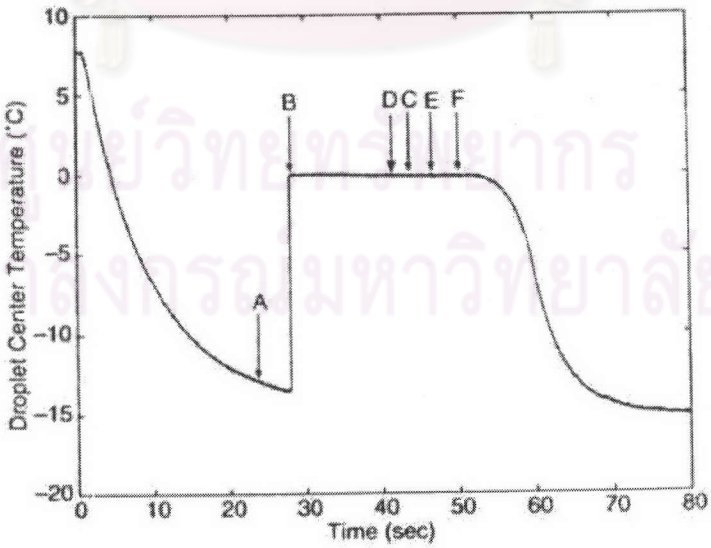

Fig. 2.42 Temperature profile of a freezing water droplet: R=0.78 mm, atmospheric temperature = -15°C and velocity = 0.54 m/s. [34]

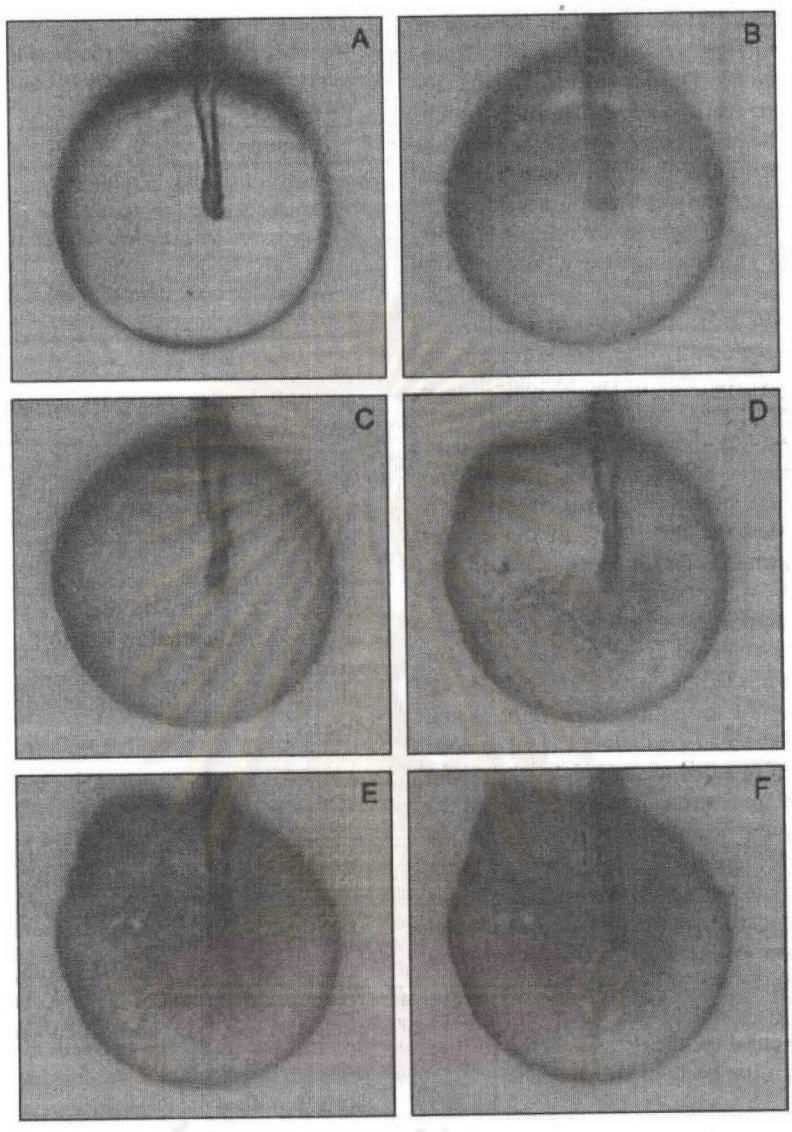

Fig. 2.43 Video frames of significant observed changes in the droplet freezing in Fig. 2.42. Time from start of cooling (A) 25 s: supercooled water, (B) 28.5 s: turns opaque immediately after nucleation, (C) 42.5 s: air bubbles first appear (below thermocouple tip), (D) 44.5 s: bulge appears on droplet, (E) 47.5 s: bulge bursts and unfrozen liquid flows onto surface, (F) 50.5 s: final frozen droplet shape, no noticeable change after this time. [34]